Available online at www.sciencedirect.com

SciVerse ScienceDirect

Geochimica et Cosmochimica Acta 104 (2013) 42–62

Geochimica et Cosmochimica Acta

www.elsevier.com/locate/gca

Pyrite as a record of hydrothermal fluid evolution in a porphyry copper system: A SIMS/EMPA trace element study

Martin Reich [a,b,*], Artur Deditius [c], Stephen Chryssoulis [d], Jian-Wei Li [e], Chan-Qiang Ma [e], Miguel Angel Parada [a,b], Fernando Barra [a,b], Florian Mittermayr [c]

[a] Departamento de Geología, Facultad de Ciencias Físicas y Matemáticas, Universidad de Chile, Santiago, Chile
[b] Andean Geothermal Center of Excellence (CEGA), Universidad de Chile, Santiago, Chile
[c] Institute of Applied Geosciences, Graz University of Technology, Graz, Austria
[d] Advanced Mineral Technology Laboratory (AMTEL), London, Ontario, Canada
[e] State Key Laboratory of Geological Processes and Mineral Resources, China University of Geosciences, Wuhan, People's Republic of China

Received 23 May 2012; accepted in revised form 2 November 2012; available online 29 November 2012

Abstract

Porphyry copper deposits are currently the world's largest source of copper and molybdenum, and are also among the largest reservoirs of gold in the upper crust. Despite the fact that pyrite is a ubiquitous mineral phase in these deposits and secondary Cu enrichment processes are commonly controlled by the abundance of this sulfide, the major and trace element chemistry of pyrite from porphyry systems remains unconstrained. In this study, we report the first comprehensive trace element database of pyrite from the Dexing deposit, China's largest porphyry Cu deposit. By combining high-spatial resolution and X-ray mapping capabilities of electron microprobe analysis (EMPA) with low detection limits and depth-profiling capabilities of secondary-ion mass spectrometry (SIMS) in a suite of samples from the Dexing deposit, we show that the concentrations of precious metals (e.g., Au, Ag), metalloids (e.g., As, Sb, Se, Te) and heavy metals (e.g., Cu, Co, Ni, Zn, Hg) in pyrite from porphyry systems are more significant than previously thought. Among the elements analyzed, Cu, As, Au and Ni are the most abundant with concentrations that vary from sub-ppm levels to a few wt.% (i.e., ~6 wt.% Cu, ~3 wt.% As, ~0.25 wt.% Au, and ~0.2 wt.% Ni). Detailed wavelength-dispersive spectrometry (WDS) X-ray maps and SIMS depth *vs.* isotope concentration profiles reveal that pyrite from the Dexing deposit is characterized by complex chemical zoning where the studied elements occur in different mineralogical forms. While As occurs as a structurally bound element in pyrite, Cu and Au can occur as both solid solution and micro- to nano-sized particles of chalcopyrite and native Au (or Au tellurides), respectively, indicating that pyrite can control metal speciation and partitioning during porphyry Cu mineralization. The well-developed oscillatory zoning detected in pyrite, where Cu-rich, As-depleted growth zones alternate with Cu-depleted, As-rich layers, indicates that Cu is geochemically decoupled from As, suggesting that this selective partitioning of metals into pyrite is most likely the result of changes in hydrothermal fluid composition.

1. INTRODUCTION

Pyrite is the most abundant sulfide in the Earth's crust and is also a major constituent of hydrothermal mineralization in a wide variety of ore systems, including porphyry copper deposits, volcanogenic massive sulfide deposits, iron-oxide–copper–gold deposits, sedimentary-hosted copper/uranium deposits, Archean to Mesozoic lode, epithermal and Carlin-type gold deposits, among others. In hydrothermal systems, pyrite is not only a sink for iron and sulfur as it also plays an important role in supergene Cu enrichment and acid mine drainage. Additionally, pyrite can contain minor elements such as Au, Ag, Cu, Pb,

* Corresponding author at: Departamento de Geología, Facultad de Ciencias Físicas y Matemáticas, Universidad de Chile, Santiago, Chile. Tel.: +56 2 9784986.
E-mail address: mreich@ing.uchile.cl (M. Reich).

0016-7037/$ - see front matter © 2012 Elsevier Ltd. All rights reserved.
http://dx.doi.org/10.1016/j.gca.2012.11.006

Zn, Co, Ni, As, Sb, Se, Te, Hg, Tl, and Bi (Cook and Chryssoulis, 1990; Fleet et al., 1993; Huston et al., 1995; Hannington et al., 1999; Large et al., 1999, 2009; Palenik et al., 2004; Vaughan and Kyin, 2004; Reich et al., 2005, 2006; Yamaguchi and Ohmoto, 2006; Barker et al., 2009; Cook et al., 2009a,b; Deditius et al., 2009a,b, 2011; Sung et al., 2009; Koglin et al., 2010; Ulrich et al., 2011). As exemplified in the Carlin-type deposits of Nevada, the second largest gold concentration in the world, gold can concentrate up to 10,000 ppm in arsenian pyrite, $Fe(S,As)_2$ (Cline et al., 2005; Muntean et al., 2011). In addition, recent investigations in pyrite from Carlin-type and epithermal gold deposits using transmission electron microscopy (TEM), secondary-ion mass spectrometry (SIMS) and electron microprobe analysis (EMPA) techniques have documented the presence of a wide variety of trace metals (i.e., Cu, Co, Pb, Sb, As, Ag, Ni, Zn, Se, Te, Hg) that occur in solid solution and/or cluster into metal nanoparticles or nano-inclusions (<100 nm size) (Deditius et al., 2008, 2009a, 2011). These findings not only provide constraints on mineral/fluid partitioning of metals and saturation state of hydrothermal solutions but also improve our knowledge about the fate of metals during environmental processes (Van Geen et al., 1997; Hochella et al., 1999; Matlock et al., 2002; Hough et al., 2008; Ciobanu et al., 2009; Cook et al., 2009a,b, 2011; Reich et al., 2010, 2011).

Porphyry copper deposits (PCDs) are currently the world's largest source of copper, and are characterized by low-grade copper, with minor gold and/or molybdenum mineralization developed within and around a porphyry intrusive complex and associated with pervasive zones of hydrothermal alteration (Kerrich et al., 2000; Sillitoe, 2000, 2010; Richards, 2003). Hydrothermal alteration in PCDs reflects changes in the host-rock mineralogy in response to water/rock interactions that occur after porphyry intrusion, and is typically zoned from an inner, high temperature potassium-silicate core surrounded by a propylitic shell, overprinted by phyllic (quartz–sericite) and argillic alteration (Lowell and Guilbert, 1970; Gustafson and Hunt, 1975; Seedorff et al., 2005). Although pyrite is abundant in PCDs, the pyrite–ore mineral paragenesis varies widely within and between deposits. Pyrite can be formed in the potassic alteration stage by sulfidation of the iron component of igneous biotite (Eq. (1)), but it is most often found with sericite and quartz forming phyllic alteration assemblages, as a result of sulfidation of iron and feldspar hydrolysis (Eq. (2)) (Beane, 1982; Beane and Bodnar, 1995; Harris and Golding, 2002; Pirajno, 2009):

$$K(Mg_{0.6}Fe^{2+}_{0.4})AlSi_3O_{10}(OH)_2 + 0.4S_2 = 0.2KMg_3AlSi_3O_{10}(OH)_2 + 0.4FeS_2 + 0.8KAlSi_3O_8 + 0.8H_2O + 1.2O_2 \quad (1)$$

$$3KAlSi_3O_8 + Fe^{2+} + 2H_2S + O_2 = KAl_3Si_3O_{10}(OH)_2 + FeS_2 + 6SiO_2 + 2K^+ + 2H_2O \quad (2)$$

In PCDs, pyrite commonly occurs in veins associated with quartz and sericite that cut previous Cu-bearing quartz veins with potassic alteration, and its abundance increases from, e.g., zones with <1–0.5 wt.% pyrite in the central part of the deposit, through a surrounding zone with up to 4 wt.%, to an outer zone with >4 wt.% (Nielsen, 1968; Gustafson and Hunt, 1975; John, 1978; Gustafson and Quiroga, 1995; Seedorff et al., 2005; Rusk et al., 2008).

Although several studies have focused on pyrite in the last decades, the major and trace element chemistry of pyrite from PCDs remains poorly understood. Surprisingly, microanalytical data of pyrite for PCDs are very limited, and available data are mostly restricted to precious metals (Au) and platinum group element (PGE) concentrations in this mineral. Among these studies, Pasava et al. (2010) documented Au and PGE in pyrite from the Kalmakyr porphyry Cu–Au–Mo deposit in Uzbekistan, and Hanley et al. (2009, 2010) reported that Co–Ni-bearing pyrite is an important repository of PGE in alkalic porphyry Cu–Au deposits from the Canadian Cordillera, with at least 90% of the bulk Pd and Pt being hosted within this mineral.

In this paper, we report the first comprehensive major and trace element database of pyrite from a porphyry copper deposit. *In situ* concentrations of precious metals (e.g., Au, Ag), metalloids (e.g., As, Sb, Se, Te) and heavy metals (e.g., Cu, Co, Ni, Zn, Hg) in a suite of pyrite samples from the Dexing deposit, China's largest porphyry Cu deposit, were determined using a combination of electron microprobe analysis (EMPA) and secondary-ion mass spectrometry (SIMS). We show that Cu, As and Au are selectively partitioned into pyrite as structurally bound metals or mineral micro/nano-particles, reaching concentrations of up to 1000 ppm at the top of the ore system. We explore the potential role of pyrite as an efficient scavenger of metals and as a monitor of changes in fluid composition in porphyry Cu systems.

2. SAMPLES AND METHODS

2.1. Pyrite samples from the Dexing Cu deposit

The Dexing deposit is the largest porphyry Cu deposit in China with ~1200 Mt of ore at 0.5% Cu, 0.01% Mo and 0.19 g/t Au (Mao et al., 2011). The deposit is located in the northeast of the Neoproterozoic Jiangnan orogenic belt and in the NW margin of the late Mesozoic magmatic belt that covers a vast area of the Cathaysia Block in SE China (Wang et al., 2006; Li and Sasaki, 2007; Mao et al., 2011) (Fig. 1A). The Jiangnan orogenic belt, also known as Jiangnan fold belt, resulted from the collision of the Yangtze Craton and the Cathaysian Block at ca. 830 Ma (Zhao et al., 2011), and consists of the metamorphic basement of the Proterozoic Banxi Group underlain by thick Paleozoic marine deposits and Mesozoic terrestrial sequences, intruded by Late Permian to Triassic peraluminous granites and syenites, as well as Jurassic and Cretaceous granitoids. The Jurassic-Cretaceous magmatism has been interpreted as a result of the north-westward subduction of the Paleo-Pacific plate beneath the Eastern China continental margin or within-plate extensional magmatism (Wang et al., 2006; Zhou et al., 2006).

The Dexing deposit is located within a ENE-trending ductile shear zone and is composed of three Cu–Mo–Au mineralized porphyries (Zhushahong, Tongchang, and

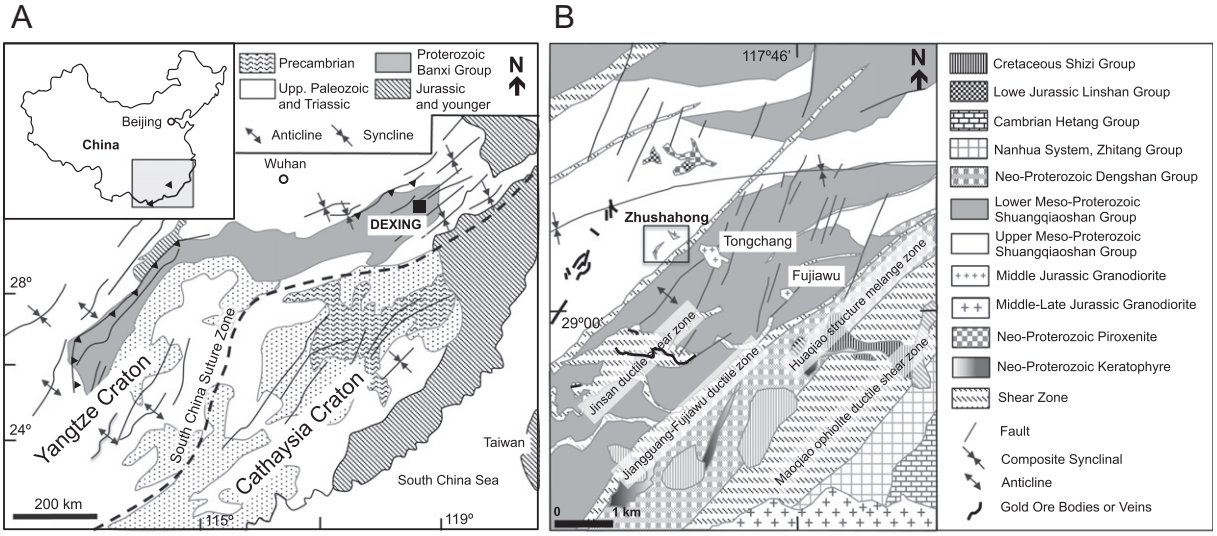

Fig. 1. (A) Location and geologic/tectonic setting of the Dexing porphyry Cu–Mo–Au deposit, southeastern China. (B) Geology of ore deposits in the Dexing area, including the Zhushahong ore body where pyrite samples for this study were taken. Geologic maps were modified after Li and Sasaki (2007).

Fujiawu), and mineralization in Proterozoic pelitic schists surrounding these intrusions (Fig. 1B). These porphyries occur as isolated stocks emplaced in the intersection of NWW- and NE-trending faults at ca. 171 Ma (Wang et al., 2006; Mao et al., 2011). Early alteration and mineralization is composed of A veins (quartz + Kspar + sulfides) and disseminated potassic alteration assemblages, followed by transitional B-type veins (quartz + molybdenite + chalcopyrite), which are cut by a late D-vein composed of abundant pyrite and minor quartz with or without sericite (Li and Sasaki, 2007). Primary fluid inclusions in quartz from the phyllic alteration assemblages (D-veins) include liquid-rich inclusions ($T \sim 115$–353 °C; 2–9 wt.% $NaCl_{equiv.}$), vapor-rich inclusions (near-critical density; ~6–16 wt.% $NaCl_{equiv.}$), and halite-bearing inclusions ($T \sim 230$–430 °C; 35–51 wt.% $NaCl_{equiv.}$). Estimated pressures for D-vein formation range between 20 and 400×10^5 Pa. More detailed descriptions and data of the deposit and district can be found in Li and Sasaki (2007) and Mao et al. (2011).

Samples for this study come from the Zhushahong porphyry (Fig. 1B) and were obtained from a subvertical 1 km drillcore penetrating the orebody, which comprises several smaller *en-echelon* ore zones (Mao et al., 2011). Five sets of massive pyrite samples from the quartz–sericite alteration assemblage (D-veins) were taken at 190, 270, 380, 550 and 800 m below the surface (samples PY-190–PY-800).

2.2. EMPA and SIMS methods

The chemical composition of pyrite was determined by electron microprobe analysis (EMPA) using a Jeol JXA8200 at the Montan University Leoben, Austria. Elements and X-ray lines used for analysis are Fe (Kα), S (Kα), As (Lα), Au (Lα), Pb (Mα), Bi (Mβ), Se (Lα), Ag (Lα), Hg (Lα), Zn (Kα), Cu (Kα), Ni (Kα), Co (Kα), Sb (Lα), and Te (Lα). Operating conditions included an accelerating voltage of 20 kV and beam current of 20 nA, and the electron beam was ~1 μm in diameter. In order to improve count rate statistics, counting times were 20 s for Fe and S, 60 s for As, Cu, Ni, Zn, and Co and 100 s for Pb, Se, Ag, Sb, Te, Au, Hg, and Bi. Standard specimens used for calibration were FeS_2 (for Fe and S), GaAs (for As), Sb_2S_3 (for Sb), HgS (for Hg), PbS (for Pb), ZnS (for Zn), $CuFeS_2$ (for Cu), $AuTe_2$ (for Au and Te), $AgBiSe_2$ (for Ag), Bi_2Se_3 (for Bi and Se), $(Ni,Fe)_9S_8$ (for Ni), and $CoAs_3$ (for Co). All of the standards (natural and synthetic) were tested for homogeneity before their utilization for quantitative analysis. Wavelength-dispersive spectrometry (WDS) X-ray maps were collected using accelerating voltage of 20 kV, beam current of 50 nA, and a counting time of 30 ms/step. The WDS scans were performed against synthetic and natural materials to avoid interference on the peak and background for (K, L, M)-lines during major and trace elements analyses. Such an approach is particularly important when analyzing trace elements that require maximum X-ray counts, and minimum or no interference to obtain accurate results. Here we report interferences that may be of broader interest during analyses of Au-bearing pyrite: Au was analyzed using Au Lα on LIF to avoid interferences between Au Mα, Mβ lines and Hg Mβ and Te Lα, respectively, noted on PETH; Hg Lα on LIF crystal instead of PETH to avoid interference with Au Mβ; Te Lα on LLIF to avoid contribution from Ni Kα on PETH. The Bi Mβ line was used instead of Bi Mα, to avoid interference with Pb Mβ. The correction factor for Pb Mα for contribution from S Kα was applied.

Secondary-ion mass spectrometry (SIMS) analyses of pyrite were performed at the Advanced Mineral Technology Laboratories (AMTEL) in London, Ontario, Canada. Because of its high accuracy and sub-ppm sensitivity, the

SIMS method allows the detection of trace elements below the ~100–300 ppm level, which is the average detection limit of EMPA. Gold, As, Cu, Ag, Sb, Te, Se and Co concentrations were obtained using a Cameca IMS-3f ion microprobe with a 10 kV and 10 nA primary Cs^+ beam source and a 4.5 kV accelerating voltage for the negative secondary ions with a 15 μm spot size, and a 2.5–5 μm depth of analyses for profiling (10–20 cycles). The ions analyzed were $^{197}Au^-$, $^{75}As^-$, $^{63}Cu^-$, $^{109}Ag^-$, $^{123}Sb^-$, $^{128,130}Te^-$ and $^{78,80}Se^-$. In addition, major constituent ions of pyrite were monitored ($^{34}S^-$ and $^{56}Fe^-$), and interferences were eliminated by 180 eV offset with the energy slit fully open. The minimum detection limits at 2σ of the background level were 100 ppb for Au, 0.1 ppm for As, 600 ppb for Cu, 3.8 ppm for Ag, 7.1 ppm for Sb, 300 ppb for Te, 30 ppb for Se, and 300 ppb for Co. In order to distinguish between the solid solution and nanoparticulate form of trace metals in pyrite, depth–concentration-profile analyses were performed on selected grains (Chryssoulis, 1990), where the pyrite matrix isotopes (^{56}Fe, ^{34}S) and the trace elements of interest (e.g., ^{63}Cu, ^{197}Au) were monitored as a function of time.

In this study, EMPA and SIMS are used as complementary techniques. Along with LA-ICP-MS (e.g., Cook et al., 2011), SIMS is currently one of the most sensitive techniques for detecting ppm-to-ppb concentrations of trace metals in sulfides (Chryssoulis et al., 2004). Since SIMS sputters into the surface, i.e., few angstrom-thick layers, over the area of few tens of micrometers, and the electron beam of ~1 μm of EMPA excites a few micrometers cubed, very different volumes of pyrite are analyzed. Therefore, slightly higher concentrations of metals such as Au have been reported for EMP analyses compared to SIMS or LA-ICP-MS (Benzaazoua et al., 2007). However, results of analyses using both methods are comparable and allow assessment of quantitative EMPA and SIMS measurements (e.g., Benzaazoua et al., 2007).

3. RESULTS

3.1. Chemical composition of pyrite

At the uppermost levels of the deposit (i.e., samples PY-190, PY-270, and PY-380), pyrite is associated with coarse-grained carbonates that fill fractures between pyrite aggregates, and/or a mixture of carbonates and sericite that formed after primary plagioclase. The amount of sericite increases with depth. On the other hand, the original mineralogy of the host rock (i.e., quartz, pyroxene and olivine) was identified in samples PY-550 and PY-800. EMP analyses of pyrite from the Dexing deposit are summarized in Appendix 1A–E, and individual spot analyses using SIMS are shown in Appendix 2.

Among all the analyzed elements, As and Cu are the most abundant in pyrite, with concentrations that are highly variable ranging from ~0.1 ppm to 2.6 wt.% (26,000 ppm), and from ~0.1 ppm to 5.9 wt.% (59,000 ppm), respectively (Appendices 1A–D and 2). The highest concentrations of these elements are found in the uppermost samples, i.e., samples PY-190, 270 and 380 (100–1000 ppm As and Cu, see Appendix 1A–C), whereas deeper samples contain less than 100 ppm As and Cu (see SIMS data, samples PY-550 and 800, Appendix 2). As shown in Fig. 2A, Cu contents do not correspond with As, as high amounts of Cu (e.g., 1000 ppm) are commonly related to low concentrations of As (e.g., 1 ppm), and vice versa. Arsenic shows a distinctive negative correlation with S ($r^2 = 0.83$, Fig. 2B), while the plot of Cu *vs.* Fe displays a nearly vertical distribution, with no clear correlation between these two elements ($r^2 = 0.12$, Fig. 2C).

Aside from As and Cu, significant Au contents were detected in all pyrite samples (Fig. 2D, Appendices 1A–D and 2). Gold in pyrite is detectable by EMPA, and has concentrations as high as ~800 ppm, with one single-spot analysis reaching 2500 ppm (sample PY-550, Appendix 1D). No evident relation was observed between high concentrations of Au (as measured by EMPA) and sample depth, although in the lower ranges of Au concentrations (<10 ppm, SIMS), the highest values are observed in the uppermost samples (e.g., PY-190, up to 10 ppm of Au), whereas deeper samples always contain ppb-levels of Au (see Appendix 2). There is a broad correspondence of Au with Cu and As, as shown in Fig. 2D and E, respectively. In addition, all samples contain hundreds of ppm levels of Hg and Ni (Appendix 1A–D). Mercury reaches a maximum content of ~1200 ppm, which is most likely related to micro-inclusions of HgS or other Hg-bearing sulfides (PY-270, Appendix 1B), and its concentrations do not vary significantly with depth nor correlate with Au, which rule out Au–Hg amalgam. Relatively high amounts of Ni were found in the upper portion of the deposit (up to 2000 ppm; sample PY-190), whilst the rest of the samples cluster around 100–200 ppm with no visible correlation ($r^2 = 0.001$, Fig. 3F, Appendix 1D). The concentrations of Co, Ag, Sb, Zn, Se, and Te are low in the analyzed pyrites and range from high ppb-levels to a few hundreds of ppm (Appendices 1A–D and 2). Among these elements, Co is the most abundant and varies from sub-ppm concentrations to ~500 ppm, whereas Ag was barely detected using EMPA (SIMS concentrations varying between ~1 and 50 ppm, Appendix 2). Antimony, Zn, Se and Te occur in low abundance, with maximum concentrations of a few hundred ppm as detected by EMPA, but commonly between 1 and 50 ppm (Appendix 2). None of these elements shows a significant correspondence with depth.

3.2. Textural and chemical features of pyrite

Back-scattered electron (BSE) imaging of the Dexing samples shows that pyrite is characterized by complex textural features that are closely related to chemical composition. Three main generations of pyrite are observed in the samples: (i) anhedral, trace element-poor (except Ni) pyrite cores ("Pyrite-I", Fig. 3G–I); (ii) coarse grained pyrite with As and Cu zoning ("Pyrite-II", Fig. 3A–F); and (iii) fine-grained pyrite ("Pyrite-III", Fig. 3D and E).

Pyrite-II is the most abundant variety, and has complex internal textures characterized by chemical zoning, abundant inclusions and variable degrees of porosity. The dominant micro-textures correspond to growth and sector zones

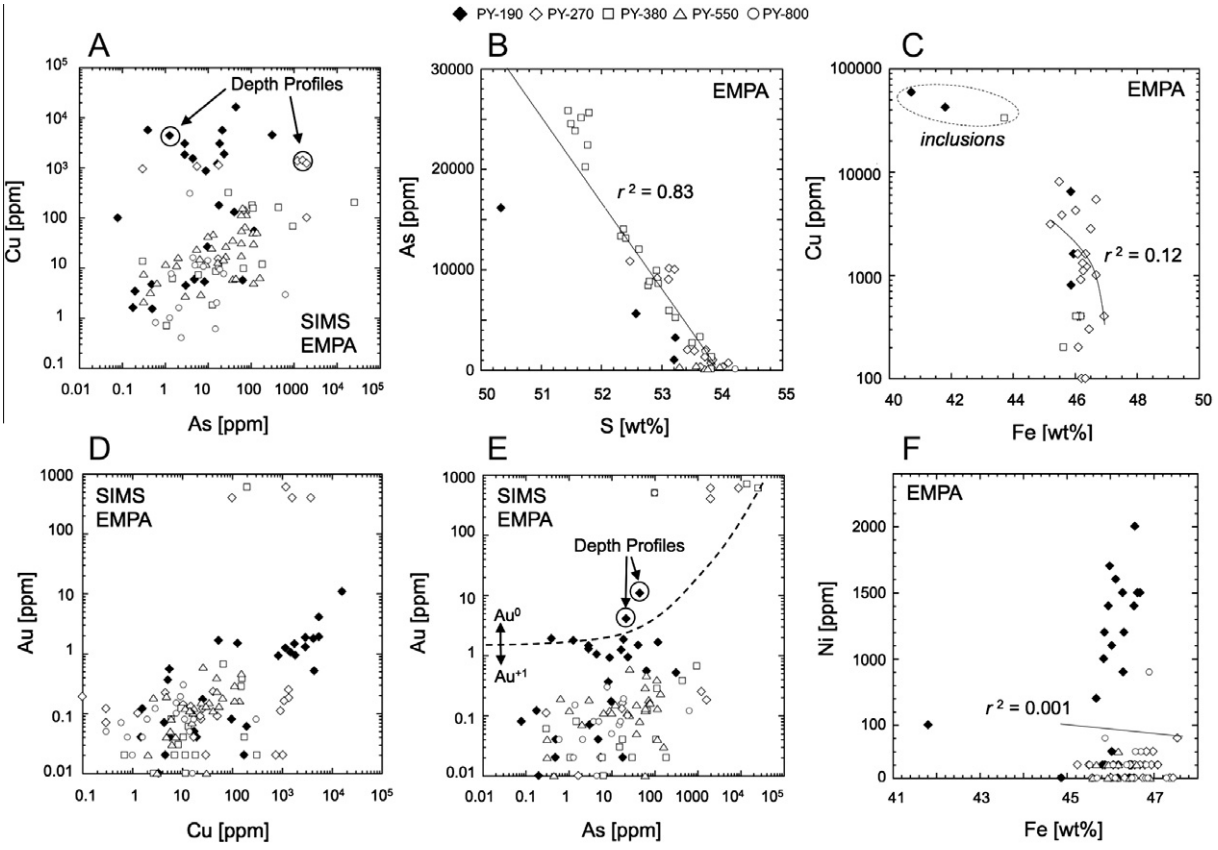

Fig. 2. Elemental diagrams for pyrite: (A) Cu *vs.* As, circled analyses correspond to SIMS depth profiles (see Fig. 5A and B); (B) As *vs.* S; (C) Cu *vs.* Fe; (D) Au *vs.* Cu; (E) Au *vs.* As, circled analyses correspond to SIMS depth profiles (Fig. 5C and D). The dashed curve represents solubility limit of Au as a function of As concentrations, as determined by Reich et al. (2005). Data-points above the line contain Au^0 (particulate), while samples below the line contain Au^{+1} (solid solution); (F) Ni *vs.* Fe. Source/s of the data (SIMS, EMPA) is/are indicated.

that are <1–500 μm thick, enriched with Cu or As (>1000 ppm) and other trace metals (e.g., Au), which alternate with pyrite zones depleted in these elements (Fig. 3A–F). Wavelength-dispersive spectrometry (WDS) X-ray maps show that these finely spaced multiple growth zones are enriched in either Cu or As, revealing a strong inverse spatial correspondence between these two elements in pyrite (Fig. 3B and C). For example, the narrow growth zones are enriched with Cu (max. 1600 ppm), Ni (max. 2000 ppm), and Hg (max. 800 ppm), but depleted in As and Au (below detection limit), and vice versa (Fig. 3A–C). Pyrite-I is defined by trace element-poor porous pyrite cores that are surrounded by inclusions-rich growth zones with variable porosity (Fig. 3G–I). Some of the growth zones in Pyrite-I are porous, thicker (up to 500 μm), and contain abundant Cu, occurring between the core of a pyrite grain and its rims (Fig. 3G–I), with numerous inclusions of chalcopyrite associated with porosity. In addition, elongated bleb-like, 10 μm × 50 μm chalcopyrite inclusions are recognized, which form ordered textures that outline the euhedral shape of pyrite crystals (Fig. 3D–F).

Pyrite-III occurs as aggregates of fine-grained, <1–100 μm pyrite crystals that grow on the surface of Pyrite-II grains, and in the interstices between them (Fig. 3D and E). The concentrations of trace elements (i.e., Cu, As, Au, Hg, Ni, etc.) are variable in Pyrite-III, with a few analyses showing Au concentrations of <700 ppm, which most likely reflect contamination from "invisible" inclusions of native Au.

4. DISCUSSION

4.1. Speciation and solubility of trace metals: solid solution *vs.* mineral inclusions

Pyrite is ubiquitous in most hydrothermal systems, and its precipitation can effectively control the partitioning of a wide array of trace elements of economic and environmental importance, such as Au, Ag, As and heavy metals (Deditius et al., 2008; Large et al., 2009). Recent studies have documented that they can occur as structurally bound elements (i.e., in solid solution), and/or as micro- to nano-sized mineral inclusions (Cline, 2001; Palenik et al., 2004; Reich et al., 2005; Barker et al., 2009; Deditius et al., 2009a, 2011). Therefore, a precise determination of the trace metal speciation in pyrite, either by analytical observations (EMPA, SIMS, TEM, LA-ICP-MS, Cook et al., 2009a, 2011; Deditius et al., 2011; Reich et al.,

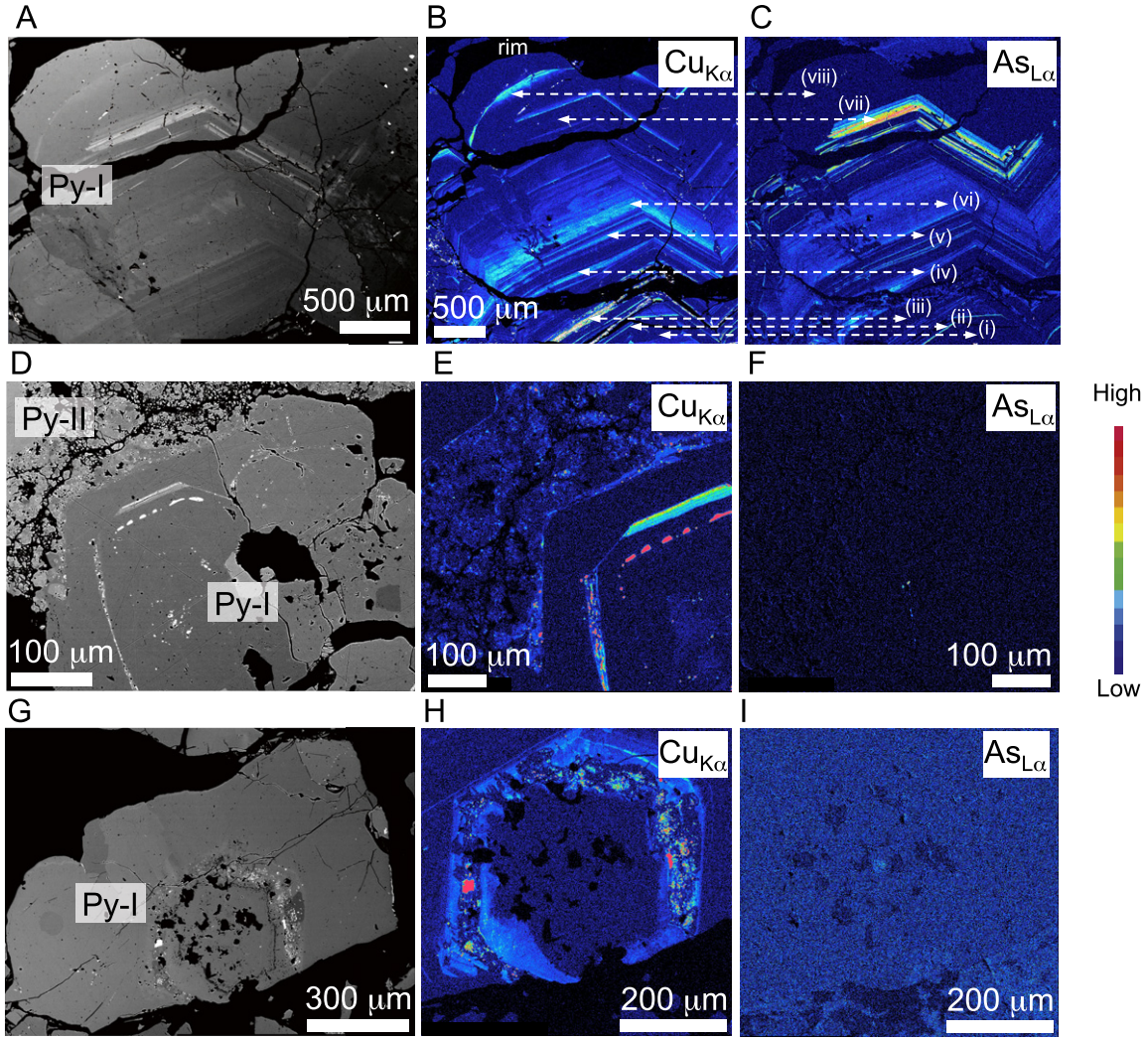

Fig. 3. Representative BSE images and WDS X-ray elemental maps of pyrite from the Dexing deposit, China. (A–C) Sample PY-270. Coarse-grained, trace-element-rich zoned pyrite ("Pyrite-II"), showing oscillatory zoning; zones "bright" in BSE are enriched with Cu and/or As. From core to rim, WDS maps of CuKα and AsLα display multiple Cu-rich growth zones that alternate with As-rich zones and zones of "barren" pyrite. Horizontal segmented lines show that Cu is decoupled from As, as Cu-rich zones associate with As-depleted zones, and vice versa (e.g., viii and vii, respectively); see text for detailed description. (D–F) Sample 190. Trace element-rich Pyrite-II followed by fine-grained Pyrite-III. The elemental map of Cu displays alternate growth and sector zoning of Cu-rich and "barren" pyrite. Copper was sequestered into the pyrite core as solid solution + few inclusions; subsequently, two generations of chalcopyrite were deposited (E). Note only few inclusions of As-rich sulfides in the center of the pyrite grain (F). (G–I) Sample 270. Core of Pyrite-I (dark patches represent qtz and feldspars) rimmed by a thick, porous Cu-growth zone. Note that Cu concentration in solid solution (light blue) increases progressively from the core to the growth zone that hosts numerous inclusions of chalcopyrite. A new layer of Cu incorporated into solid solution is formed after the chalcopyrite-bearing zones, with outward decreasing concentrations outwards. (For interpretation of the references to colour in this figure legend, the reader is referred to the web version of this article.)

2010) or spectroscopic determinations (e.g., synchrotron XANES-EXAFS; Simon et al., 1999; Savage et al., 2000) has been proved to be critical for understanding the processes responsible for metal partitioning during ore formation, and also to better assess the release of metals during weathering.

At the Dexing porphyry Cu deposit, As, Cu and Au are the most abundant metals in pyrite. The studied pyrite can be classified as "arsenian" in terms of As contents (i.e., up to wt.% levels), indicating that the concentration of this element can be significant in porphyry Cu systems. The scarcity of As-bearing inclusions or nanoparticles, coupled to a well-defined inverse correlation between As and S (Fig. 2B), strongly suggests that As in the studied pyrites is substituting for S in the pyrite structure as anionic As^{1-} as previously reported for reducing environments, and unlike in more oxidized, shallower systems where As can occur as As^{3+} in pyrite (e.g., epithermal Au deposits) (Simon et al., 1999; Cline, 2001; Emsbo et al., 2003; Reich et al., 2005; Deditius et al., 2008, 2009a, 2011; Morey et al.,

2008). Therefore, most of the As in pyrite at Dexing is distributed in the same oxidation state (1−), and no variations in As-speciation in pyrite are observed with depth.

Unlike As, very few studies have documented high Cu concentrations in pyrite, also known as "cuprian pyrite". Although it is commonly accepted that most Cu occurs in pyrite as inclusions of Cu-sulfides (e.g., chalcopyrite), studies have reported that Cu can be accommodated within the pyrite structure in significant amounts, in some cases reaching wt.% levels (Frenzel and Ottemann, 1967; Einaudi, 1968; Clark, 1970; Radcliffe and McSween, 1970; Pacevski et al., 2008). In hypogene Cu deposits, copper is usually supersaturated with respect to Cu-bearing sulfides forming chalcopyrite ($CuFeS_2$), bornite (Cu_5FeS_4) and chalcocite (Cu_2S). The high contents of Cu reported in pyrites from the Dexing deposit, which can reach up to ~6 wt.%, indicate that pyrite may act as an important Cu scavenger in porphyry Cu deposits, and therefore may play an unforeseen control on this element during ore system evolution.

At the Dexing deposit, detailed EMPA observations, WDS X-ray mapping and SIMS depth profiles reveal that Cu in pyrite occurs in two dominant mineralogical forms: (i) as structurally bound Cu, and (ii) as micro- to nano-sized inclusions of chalcopyrite. Both forms of Cu can be observed in Fig. 3B–E and H and in Fig. 4. In Fig. 4, a ~50 μm growth zone is displayed at different magnifications on BSE images, along with WDS X-ray maps of Cu, Ni, Fe and S. Structurally bound Cu is distributed homogeneously forming the light blue-colored bands that define the edge of the growth zone, contrasting with the dark-blue, low-Cu background of the pyrite grain (Fig. 4B, CuKα WDS map). The high-Cu, solid solution light-blue band is related to the yellow-orange band in Fig. 4D and E (FeKα and SKα WDS maps), which is characterized by lower Fe and S than the average pyrite matrix (dark orange high-Fe pyrite background). Although the elemental correlation between Cu and Fe in Fig. 2C is not fully conclusive to support a direct $Cu^{2+} \leftrightarrow Fe^{2+}$ substitutional mechanism in the FeS_2–CuS_2 join (Shimazaki and Clark, 1970; Schmid-Beurmann and Bente, 1995), it is likely that most of the structurally bound Cu replaces Fe in octahedral sites. This may be due to considerable distortion of the pyrite symmetry by the presence of the other elements like As, Sb or Co (Radcliffe and McSween, 1969; Bayliss, 1989). On the other hand, micro- to nano-sized Cu-bearing inclusions occur as scattered yellow-to-red-colored discrete particles and blebs along the growth zones (Fig. 4D). The size of the particles varies from ~25 μm to <1 μm, and they occur as individual inclusions and/or as aggregates of abundant micrometer to submicrometer-sized particles. Single, Cu-rich particles and aggregates correlate with lower-than-background (Fe, S)-depleted spots, indicating that most of the Cu is contained in the form of chalcopyrite or other Cu sulfides and sulfosalts. The occurrence of the two mineralogical forms of Cu in pyrite at Dexing is confirmed by SIMS depth profiles, where each successively deeper layer of the material is analyzed as a function of time. In Fig. 5A and B, depth–concentration profiles (time *vs.* intensity in counts per second) are presented for the pyrite matrix isotopes (^{56}Fe, ^{34}S), and copper (^{63}Cu). When Cu is present in solid solution (structurally bound), the depth–concentration profile of ^{63}Cu is flat (Fig. 5, 1400 ppm Cu, see Fig. 2A), whereas at higher concentrations the spiky ^{63}Cu profile confirms the presence of individual particles or clusters of particles of ~500 nm in size (Fig. 5, 4300 ppm Cu, see Fig. 2A).

The previous textural and chemical observations indicate that the analyzed pyrites can only host a limited amount of

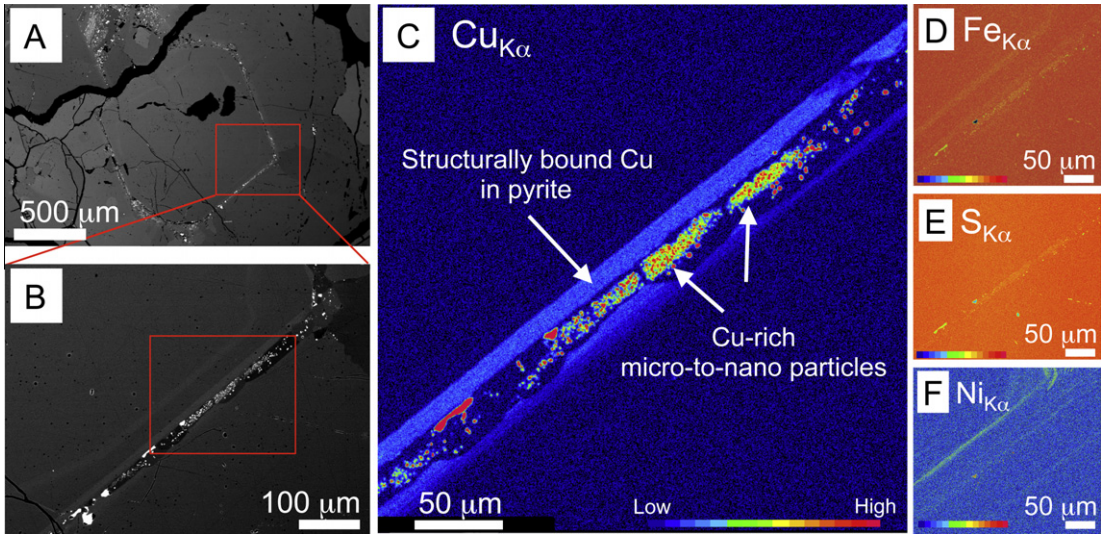

Fig. 4. Back-scattered electron (BSE) images (A and B) and detailed wavelength-dispersive spectrometry (WDS) X-ray elemental maps of a Cu-rich growth zone (C–F). Elemental mapping shows that Cu occurs in two mineralogical forms, as structurally bound Cu (light blue fringes) and as individual sub-micrometer particles of chalcopyrite that aggregate to form larger, micrometer-scale irregular and elongate particles (maps C–E). Note that Ni-rich growth zone and Ni in solid solution pre-date enrichment of pyrite in Cu. Arsenic concentrations are below the EMPA detection limit in the mapped area. (For interpretation of the references to colour in this figure legend, the reader is referred to the web version of this article.)

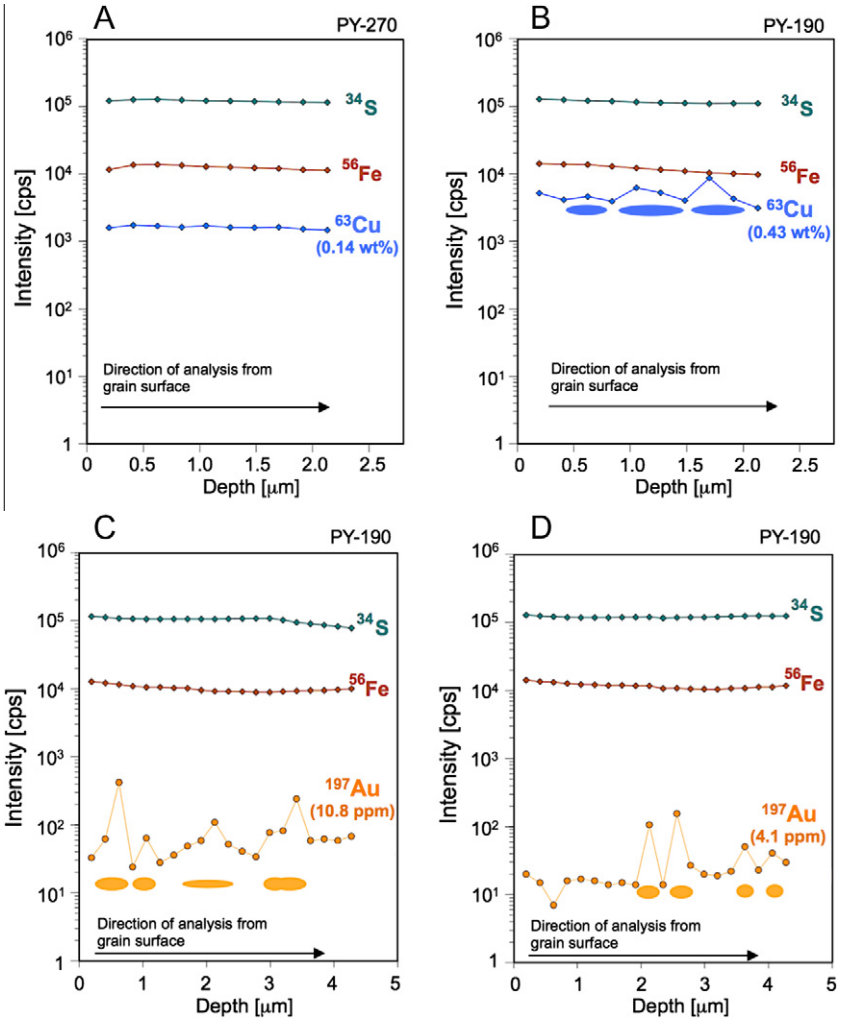

Fig. 5. SIMS depth (μm) *vs.* concentration (counts per second) profiles of selected pyrite grains from Dexing deposit. The flat ^{63}Cu profile in (A) indicates incorporation of Cu in solid solution, while the spiky profile in (B) shows the presence of Cu-rich, micro- and nano-inclusions or aggregates of smaller particles. ^{197}Au spiky profiles document micrometer-sized inclusions of native Au (or Au telluride). The analyzed spots are also shown in Fig. 2A and E.

Cu in solid solution, e.g., roughly 1000–2000 ppm as seen in Figs. 2A, 4C and 5A. WDS mapping of Cu-growth zones (Fig. 4C) suggests that when this solubility limit is surpassed during pyrite growth from a hydrothermal fluid, Cu-bearing sulfide (chalcopyrite) nanoparticles nucleate in the Cu-saturated fluid at or close to the pyrite–fluid interface. They form single nanoparticles and/or clusters of nanoparticles that aggregate to form larger, micrometer-sized Cu-bearing inclusions (Fig. 4C). Therefore, the highest concentration of Cu (e.g., >10,000 ppm) measured by EMPA and SIMS is probably related to the presence of sub-micrometer particles and nanoparticle aggregates of chalcopyrite or other Cu-bearing sulfide mineral. These observations are consistent with hydrothermal synthesis studies indicating that the solid solution of CuS_2 in FeS_2 is thermodynamically unstable in nature unless temperature and pressure exceed the conditions typical of hydrothermal alteration and pyrite formation in porphyry systems (i.e., solubility of Cu in FeS_2 increases from ~0.6 mol% Cu at 700 °C to 4.5 mol% Cu at 900 °C, at 45 kbar; Shimazaki and Clark, 1970; Schmid-Beurmann and Bente, 1995). Although the incorporation of Cu into solid solution at the levels >1000 ppm is not favored in pyrite from the Dexing deposit, a recent study by Pacevski et al. (2008) reports high concentrations of solid solution Cu in pyrite samples from the Coka Marin volcanogenic massive sulfide deposit in Serbia. These authors observed a relation between increasing Cu contents and decreasing wave numbers of Raman band positions, and an increase in the lattice parameter of pyrite as determined by X-ray diffraction. These structural variations are interpreted as the result of incorporation of up to 8 wt.% of Cu in solid solution, although colloform pyrite with abundant chalcopyrite inclusions was observed in the studied samples.

Apart from Cu and As, Au concentrations in the studied pyrite samples are relatively high (ppb to 100 ppm levels), and display a similar relationship with arsenic to the one re-

ported for (Au, As)-bearing pyrite from Carlin-type, epithermal, and mesothermal Au deposits (Cook and Chryssoulis, 1990; Arehart et al., 1993; Reich et al., 2005; Deditius et al., 2009b; Large et al. 2009). As shown in Fig. 2E, most of the Au–As analyses form a wedge-shaped zone in log–log space, with a few data points that plot above the segmented/dashed-line, defined by Reich et al. (2005) as the empirical solubility limit of Au as a function of As in pyrite. According to Reich et al. (2005), Au–As points that plot below the solubility line contain Au in solid solution as Au^{1+}, whereas samples that plot above the solubility line, Au is present as micro- to nano-sized inclusions. Fig. 2E shows that Au–As analyses from Dexing plot above and below the solubility line, suggesting that Au occurs in two mineralogical forms, i.e., as structurally bound ions (Au^{1+}) and as free particles of native Au^0 and/or Au-tellurides. This is confirmed by the spiky SIMS depth–concentration profiles that show individual particles or aggregates of nanoparticulate Au^0 (or calaverite $AuTe_2$) of sizes <1 μm (Fig. 5C and D). The results presented here indicate that most of the Au in pyrite from the Dexing deposit is contained in solid solution at concentrations <10 ppm. Higher concentrations (e.g., 100–1000 ppm Au) reported are exclusively related to micro- to nano-sized particles of Au (see Fig. 2E and Appendices 1 and 2). It is important to note that Au concentrations in pyrite at Dexing are higher than those reported by Kesler et al. (2002) for Cu–(Fe)-minerals from the Batu Hijau and Skouries porphyry Cu deposits, which show sub-ppm average Au contents. Such comparison clearly shows the importance of pyrite as a gold scavenger in high-temperature porphyry settings.

Sample PY-190 is characterized by relatively high concentrations of Ni, which form a cluster of data between ~1000 and 2000 ppm Ni (Fig. 2F). Despite the lack of correlation between Ni and Fe (Fig. 2F), it is likely that Ni occurs in solid solution in pyrite, with Ni substituting for Fe in the octahedral sites, as no Ni inclusions were observed and WDS X-ray mapping shows continuous, homogeneous Ni-rich zones (Fig. 4F). Nickel contents in pyrite are within the ranges reported for hydrothermal ore deposits, i.e., between 100 and ~3000 ppm (Campbell and Ethier, 1984; Kaneda et al., 1986; Raymond, 1996; Hanley et al., 2010). All other trace elements reported in this study (e.g., Hg, Sb, Co, Se, Te, Ag) occur in low amounts (up to a few hundred ppm) and are most likely hosted within the pyrite structure, with the exception of high concentrations of Hg (<1200 ppm), that probably reflect contamination from HgS inclusions.

4.2. Geologic implications: Cu and As decoupling in porphyry systems

The geochemistry of Cu, As and Au in the magmatic-hydrothermal environment is largely controlled by the physico-chemical properties of the fluids, and in porphyry Cu systems in particular, fluid-phase separation controls ore-metal partitioning and precipitation of sulfides/ore minerals (Heinrich, 2007, and references therein). However, for most porphyry Cu deposits, it is difficult to determine how the compositions of hydrothermal fluids change with time and how those changes affect the distribution of ore minerals (Rusk et al., 2008). At the Bajo de la Alumbrera porphyry Cu–Au deposit in Argentina, Ulrich and Heinrich (2002) combined microthermometry with LA-ICP-MS analyses of single fluid inclusions to determine the evolution of ore metal concentrations with temperature and pressure. Cooling and decompression of high-salinity fluids (50–60 wt.% $NaCl_{equiv.}$, 750 °C, $P > 1$ kbar, 0.33 wt.% of Cu and 0.55 ppm of Au) down to ~450 °C caused alteration/decomposition of K-silicate and magnetite, but no supersaturation and precipitation of Au or Cu-sulfides were observed. However, between ~400 and 300 °C, ~85% of the Cu and Au from the fluid was precipitated as chalcopyrite and native Au during potassic alteration, followed by feldspar-destructive, quartz–sericite alteration with decreasing fluid salinities and temperatures below 300 °C (Ulrich and Heinrich, 2002). Besides the large amount of data obtained from *in situ* LA-ICP-MS analysis of fluid inclusion assemblages in quartz from porphyry systems (Heinrich et al., 2005; Audétat et al., 2008), recent LA-ICP-MS studies in fluid inclusions hosted in sulfide ore minerals (e.g., Kouzmanov et al., 2010) have reported significant variations in metal concentrations related to successive pulses of chemically distinct hydrothermal fluids. Within this context, elemental mapping and microanalysis of pyrite may provide complementary information about the variation in chemical composition of hydrothermal fluids during continuous sulfide growth.

Fig. 3A–C displays an example of complex (Cu, As)-growth zoning in Pyrite-II from sample PY-270 from Dexing, consisting of tens of Cu and/or As-rich growth zones. The textural relationships indicate that, at the beginning of mineral growth, a low Cu, As-depleted pyrite core was formed (stage-(i)), followed by stage-(ii) that is marked by Cu and As enrichment (Fig. 3B and C). Subsequently, stage-(iii), a Cu-rich growth zone containing inclusions of chalcopyrite, was deposited on the pyrite surface, without detectable amounts of As. Arsenic was incorporated into pyrite during the next episode, stage-(iv). Stage-(v) is represented by a sharp and thick (~1 μm) Cu-rich, As-depleted gowth zone. Then, stage-(vi) pyrite growth was dominated by fluids enriched in both Cu and As, and formed a ~1 mm thick package of growth zones. At stage-(vii), the richest As zone was deposited, whereas Cu was depleted (<300 ppm). Finally, stage-(viii) formed two growth zones rich in Cu, preceded and followed by barren pyrite with As content below EPMA detection limits.

The observed textures at the Dexing deposit represent the first example of Cu–As oscillatory zoning in a porphyry Cu system, although similar features have been reported in pyrites from the Yanacocha and Pueblo Viejo epithermal Au and Ag–Au high-sulfidation ore deposits, respectively (Deditius et al., 2009b). Those authors reported the occurrence of As-bearing growth zones enriched with Au, Ag, Te, Sb, Te and Pb that alternated with Cu-rich zones with significantly lower concentrations of these trace elements, and "barren" pyrite growth zones. Such texture was interpreted to represent changes in the composition of the magmatic hydrothermal fluid rather than differences between

Appendix 1A
Representative EMPA analyses (wt.%) of pyrite. b.d., below detection. Detection limits (wt.%) are shown below each element.

Sample PY-190	Cu (0.01)	Fe (0.30)	S (0.20)	As (0.01)	Co (0.008)	Ni (0.01)	Zn (0.013)	Hg (0.04)	Se (0.009)	Te (0.009)	Ag (0.006)	Au (0.04)	Total
o41	b.d.	45.65	53.68	b.d.	0.01	b.d.	b.d.	b.d.	b.d.	b.d.	0.01	b.d.	99.38
o42	b.d.	46.38	53.21	b.d.	b.d.	b.d.	b.d.	b.d.	b.d.	b.d.	b.d.	0.05	99.68
o44	b.d.	45.77	53.35	b.d.	0.01	b.d.	b.d.	b.d.	b.d.	b.d.	b.d.	b.d.	99.17
o45	b.d.	45.84	53.11	b.d.	0.01	b.d.	b.d.	b.d.	b.d.	b.d.	b.d.	b.d.	99.00
o47	b.d.	46.04	52.70	b.d.	0.01	0.03	b.d.	0.05	b.d.	0.01	b.d.	b.d.	98.85
o48	b.d.	46.27	52.93	b.d.	b.d.	b.d.	b.d.	0.05	b.d.	0.01	b.d.	b.d.	99.28
o49	b.d.	46.08	53.04	b.d.	0.01	0.02	b.d.	b.d.	b.d.	b.d.	b.d.	b.d.	99.23
o50	5.89	40.72	50.34	1.61	b.d.	b.d.	0.02	0.06	b.d.	b.d.	b.d.	b.d.	98.70
o51	b.d.	46.19	52.70	b.d.	0.02	0.02	b.d.	b.d.	b.d.	b.d.	b.d.	b.d.	98.95
o52	b.d.	46.43	52.84	b.d.	0.01	b.d.	b.d.	b.d.	b.d.	b.d.	b.d.	b.d.	99.31
o53	b.d.	46.50	53.03	b.d.	0.01	0.02	b.d.	0.06	b.d.	b.d.	b.d.	b.d.	99.65
o54	b.d.	46.25	52.84	b.d.	0.02	b.d.	b.d.	0.04	b.d.	b.d.	b.d.	b.d.	99.17
o55	b.d.	46.14	53.21	b.d.	b.d.	b.d.	b.d.	b.d.	0.02	b.d.	b.d.	b.d.	99.40
o56	b.d.	46.29	53.04	b.d.	b.d.	b.d.	b.d.	b.d.	b.d.	b.d.	b.d.	0.04	99.40
o57	b.d.	46.41	52.69	b.d.	0.02	b.d.	b.d.	0.09	b.d.	0.01	b.d.	b.d.	99.23
o58	b.d.	46.40	52.65	b.d.	0.02	b.d.	b.d.	b.d.	b.d.	b.d.	b.d.	b.d.	99.11
o59	b.d.	46.22	52.41	b.d.	b.d.	b.d.	b.d.	b.d.	b.d.	b.d.	b.d.	b.d.	98.67
o60	b.d.	45.82	52.80	b.d.	b.d.	b.d.	b.d.	b.d.	b.d.	b.d.	b.d.	b.d.	98.66
o61	0.04	46.10	53.23	b.d.	0.02	b.d.	b.d.	0.05	b.d.	b.d.	b.d.	b.d.	99.47
o62	0.08	45.88	53.03	b.d.	0.03	0.02	b.d.	b.d.	b.d.	0.04	b.d.	b.d.	99.12
o63	b.d.	45.93	53.04	b.d.	0.009	b.d.	b.d.	b.d.	b.d.	b.d.	b.d.	0.06	99.05
o64	0.04	46.18	53.19	b.d.	0.02	0.01	0.01	0.04	b.d.	0.02	b.d.	b.d.	99.52
o66	b.d.	46.27	52.98	b.d.	0.01	b.d.	b.d.	b.d.	b.d.	b.d.	b.d.	b.d.	99.28
o69	b.d.	45.68	52.95	b.d.	0.02	b.d.	b.d.	0.04	b.d.	0.02	b.d.	b.d.	98.72
o70	b.d.	45.49	54.02	b.d.	0.02	b.d.	b.d.	b.d.	b.d.	0.02	b.d.	0.05	99.65
o71	b.d.	45.99	53.19	b.d.	0.05	0.17	b.d.	0.05	b.d.	b.d.	b.d.	b.d.	99.45
o72	0.64	45.87	52.67	b.d.	b.d.	0.12	b.d.	b.d.	b.d.	b.d.	b.d.	b.d.	99.33
o73	b.d.	46.30	53.22	b.d.	0.02	0.09	b.d.	b.d.	b.d.	b.d.	b.d.	b.d.	99.64
o74	b.d.	46.69	53.17	b.d.	0.01	0.15	0.01	b.d.	b.d.	0.01	b.d.	b.d.	100.11
o75	b.d.	46.55	53.11	b.d.	0.02	0.14	b.d.	b.d.	0.01	b.d.	b.d.	b.d.	99.87
o76	b.d.	46.04	53.25	b.d.	b.d.	0.11	0.02	b.d.	b.d.	b.d.	b.d.	b.d.	99.47
o77	b.d.	45.85	53.13	b.d.	0.01	0.10	b.d.	b.d.	b.d.	b.d.	b.d.	0.06	99.16
o78	b.d.	46.63	53.17	b.d.	0.03	0.15	b.d.	b.d.	b.d.	b.d.	b.d.	0.05	100.07
o79	b.d.	46.29	52.99	b.d.	0.02	0.15	0.02	b.d.	b.d.	b.d.	b.d.	b.d.	99.49
o80	0.16	45.96	52.71	b.d.	0.01	0.14	b.d.	0.08	b.d.	b.d.	b.d.	b.d.	99.08
o81	b.d.	46.13	53.17	b.d.	0.02	0.16	b.d.	0.07	b.d.	b.d.	b.d.	0.07	99.62
o83	b.d.	46.57	53.54	b.d.	b.d.	0.20	b.d.	0.08	b.d.	b.d.	0.006	b.d.	100.40
o83a	b.d.	46.32	53.08	b.d.	0.02	0.12	0.02	0.10	b.d.	b.d.	b.d.	b.d.	99.68
o84	b.d.	45.68	52.97	b.d.	0.009	0.07	b.d.	0.05	b.d.	0.02	b.d.	b.d.	98.82
o86	b.d.	46.44	53.36	b.d.	0.009	0.01	0.02	b.d.	b.d.	b.d.	b.d.	b.d.	99.87
o87	b.d.	46.17	53.21	b.d.	0.02	b.d.	b.d.	b.d.	b.d.	b.d.	b.d.	b.d.	99.45
o88	b.d.	45.83	53.43	b.d.	b.d.	0.02	b.d.	0.05	b.d.	b.d.	b.d.	b.d.	99.34
o89	b.d.	46.55	53.41	b.d.	0.009	0.01	b.d.	b.d.	b.d.	b.d.	b.d.	b.d.	100.02

(*continued on next page*)

Appendix 1A (*continued*)

Sample PY-190	Cu (0.01)	Fe (0.30)	S (0.20)	As (0.01)	Co (0.008)	Ni (0.01)	Zn (0.013)	Hg (0.04)	Se (0.009)	Te (0.009)	Ag (0.006)	Au (0.04)	Total
o91	b.d.	45.37	52.58	0.56	b.d.	b.d.	b.d.	0.04	b.d.	b.d.	b.d.	b.d.	98.59
o92	b.d.	46.49	53.27	b.d.	b.d.	b.d.	0.02	b.d.	b.d.	b.d.	b.d.	b.d.	99.79
o93	b.d.	46.46	53.40	b.d.	0.01	0.01	b.d.	b.d.	b.d.	0.01	b.d.	b.d.	99.93
o95	b.d.	45.90	53.35	b.d.	0.01	b.d.	b.d.	0.04	b.d.	b.d.	b.d.	b.d.	99.34
o96	b.d.	45.93	53.23	b.d.	0.02	b.d.	b.d.	b.d.	b.d.	b.d.	b.d.	b.d.	99.21
o97	b.d.	45.92	52.84	b.d.	b.d.	b.d.	b.d.	b.d.	b.d.	0.01	b.d.	b.d.	98.78
o99	b.d.	45.72	53.07	b.d.	0.01	0.01	b.d.	b.d.	b.d.	b.d.	b.d.	b.d.	98.87
o100	b.d.	46.12	53.23	0.32	0.01	b.d.	b.d.	b.d.	b.d.	b.d.	b.d.	b.d.	99.70
o101	b.d.	46.18	53.21	0.10	b.d.	b.d.	b.d.	b.d.	b.d.	b.d.	b.d.	b.d.	99.54
o105	b.d.	46.09	52.80	b.d.	0.03	b.d.	b.d.	b.d.	b.d.	b.d.	b.d.	b.d.	98.96

substitutional mechanisms of As and Cu from a fluid of constant composition. The evidence presented in this study indicates that the decoupled geochemical behavior of Cu and As is not exclusively restricted to the epithermal, shallower portions of hydrothermal ore systems but also can be recognized at deeper, porphyry levels. At the Dexing porphyry Cu deposit, the finely spaced multiple growth zones are representative of changes in trace-element fluid composition during the continuing deposition of pyrite, which is ubiquitous during potassic and phyllic (quartz–sericite) alteration. It is most likely that these abrupt changes in metalloid, base and precious metal concentrations during ore formation and wall-rock alteration, which are cryptically recorded in pyrite, represent changes in fluid composition resulting from mixing between magmatic vapors and hydrothermal fluids. Analytical and experimental data by several researchers (Candela and Holland, 1984; Heinrich et al., 1999, 2004; Kesler et al., 2002; Pokrovski et al., 2002, 2005; William-Jones and Heinrich, 2005; Klemm et al., 2007; Simon et al., 2007, 2008; Deditius et al., 2009b) show that vapors of magmatic and hydrothermal origin that differ in composition/s are common in porphyry systems, and that despite the fact that Cu and As are partitioned into the vapor phase, they respond differently to temperature, pressure and ligand (Cl, S) concentrations. Therefore, the geochemical decoupling of Cu and As at Dexing could be explained as the result of mixing between pyrite-forming fluids and high-temperature (~600–700 °C) As (and other trace elements)-rich vapors that invade the main hydrothermal systems repeatedly and intermittently with lower-temperature (~300 °C), Cu-rich vapors. Supersaturation with respect to Cu (chalcopyrite) and native Au (or Au tellurides) in the hydrothermal fluid close and/or at the pyrite–fluid interface during these episodic vapor incursions would result in the precipitation/deposition of metallic nanoparticles and micrometer-scale aggregates on the pyrite surface.

Previous studies have proposed that Au might be scavenged from porphyry Cu systems by high-temperature vapor phases (600–700 °C) (Kesler et al. 2002). SIMS analyses of ore and gangue minerals (bornite, chalcopyrite, chalcocite, covellite and pyrite) at the Kingking, Skouries and Batu Hijau porphyry Cu deposits revealed that bornite is the most important host of Au, containing ~1 ppm Au, whereas chalcopyrite contains at least an order of magnitude less, in the same range of average concentrations than pyrite as reported in that study (e.g., average of 0.19 ppm at Batu Hijau, and 0.5 ppm at Skouries). Based on SIMS data and phase equilibria studies in the Cu-Fe-S-Au systems, those authors suggested that a 100 °C temperature drop (e.g., between 800 and 700 °C) would decrease Au solubility in bornite and chalcopyrite from 800 to 200 ppm, releasing almost 75% of Au from the Cu–Fe sulfides. Such process may be supported by field evidence that shows a close spatial connection between the Dexing porphyry Cu deposits and the several Au ore bodies and veins that are located in the Dexing district west of the studied deposit (Fig. 1B), further indicating that Au precipitation in the epithermal environment was the result of an effective scavenging and redistribution process whereby Au was lost from an underlying porphyry Cu system.

Appendix 1B
Representative EMPA analyses (wt.%) of pyrite. b.d., below detection. Detection limits (wt,%) are shown below each element.

Sample PY-270	Cu (0.01)	Fe (0.30)	S (0.20)	As (0.01)	Co (0.008)	Ni (0.01)	Zn (0.013)	Hg (0.04)	Se (0.009)	Te (0.009)	Ag (0.006)	Au (0.04)	Total
p36	b.d.	46.79	54.17	b.d.	b.d.	b.d.	b.d.	0.12	b.d.	b.d.	b.d.	b.d.	101.10
p37	b.d.	46.44	53.55	0.19	0.01	b.d.	b.d.	0.04	b.d.	0.01	b.d.	b.d.	100.27
p38	b.d.	46.78	54.02	0.03	0.01	b.d.	b.d.	b.d.	b.d.	b.d.	b.d.	b.d.	100.86
p39	0.42	46.03	53.65	0.03	b.d.	0.01	0.02	0.06	b.d.	b.d.	b.d.	b.d.	100.27
p40	0.12	46.38	53.43	0.20	0.008	b.d.	b.d.	0.06	b.d.	b.d.	0.006	0.06	100.27
p41	0.16	46.10	53.82	0.07	0.008	b.d.	b.d.	b.d.	b.d.	b.d.	0.01	b.d.	100.18
p42	0.01	46.22	53.74	0.200	0.01	b.d.	b.d.	b.d.	b.d.	b.d.	b.d.	0.04	100.24
p43	0.02	46.12	53.81	0.11	0.02	b.d.	b.d.	0.07	b.d.	0.01	b.d.	b.d.	100.18
p44	b.d.	45.91	54.11	0.07	0.01	b.d.	0.02	b.d.	b.d.	b.d.	b.d.	b.d.	100.18
p45	b.d.	46.00	54.19	b.d.	b.d.	b.d.	b.d.	0.06	b.d.	b.d.	b.d.	b.d.	100.30
p46	b.d.	45.57	53.13	1.01	b.d.	b.d.	b.d.	b.d.	b.d.	b.d.	b.d.	b.d.	99.72
p47	b.d.	46.44	52.93	0.91	b.d.	0.02	0.02	0.07	b.d.	b.d.	b.d.	b.d.	100.38
p48	b.d.	45.52	52.48	1.08	0.01	0.02	b.d.	b.d.	b.d.	b.d.	b.d.	b.d.	99.15
p49	b.d.	45.25	53.12	0.90	0.01	0.02	b.d.	b.d.	b.d.	b.d.	b.d.	0.06	99.38
p50	b.d.	46.48	53.22	1.00	b.d.	0.02	0.01	0.05	0.01	b.d.	b.d.	b.d.	100.82
p51	b.d.	46.47	53.58	b.d.	0.01	0.02	b.d.	0.05	b.d.	b.d.	b.d.	b.d.	100.15
p52	0.31	45.21	53.85	b.d.	b.d.	b.d.	b.d.	b.d.	b.d.	b.d.	b.d.	b.d.	99.40
p53	0.38	45.59	53.73	b.d.	0.01	0.01	0.01	0.05	b.d.	b.d.	b.d.	0.04	99.83
p54	b.d.	46.80	53.81	b.d.	b.d.	0.02	b.d.	b.d.	0.01	0.01	b.d.	b.d.	100.69
p55	b.d.	46.69	53.74	b.d.	0.008	0.02	b.d.	0.07	b.d.	b.d.	b.d.	b.d.	100.58
p56	0.11	46.27	53.89	b.d.	b.d.	b.d.	b.d.	0.06	b.d.	0.01	b.d.	b.d.	100.39
p57	0.16	46.35	53.89	b.d.	b.d.	0.01	b.d.	b.d.	b.d.	b.d.	b.d.	0.04	100.46
p58	0.28	46.52	53.72	0.13	0.01	b.d.	b.d.	0.05	b.d.	b.d.	b.d.	b.d.	100.75
p59	0.13	46.25	53.85	0.10	0.02	b.d.	b.d.	0.05	b.d.	0.01	b.d.	b.d.	100.44
p60	0.10	46.69	53.83	0.02	b.d.	0.02	b.d.	b.d.	b.d.	0.01	b.d.	b.d.	100.71
p61	0.04	46.95	52.98	b.d.	0.01	0.02	0.02	b.d.	b.d.	b.d.	b.d.	b.d.	100.05
p62	b.d.	46.57	53.76	b.d.	0.01	0.02	b.d.	b.d.	0.01	0.02	b.d.	b.d.	100.46
p63	0.03	46.46	53.63	b.d.	b.d.	0.02	b.d.	0.04	b.d.	b.d.	b.d.	b.d.	100.22
p64	b.d.	47.55	53.79	b.d.	b.d.	0.04	b.d.	b.d.	b.d.	b.d.	b.d.	0.04	101.45
p65	b.d.	47.37	53.95	b.d.	b.d.	0.01	0.01	b.d.	b.d.	b.d.	b.d.	b.d.	101.36
p66	b.d.	46.56	53.98	b.d.	b.d.	b.d.	b.d.	b.d.	b.d.	0.01	b.d.	b.d.	100.59
p67	b.d.	46.90	54.05	b.d.	0.01	b.d.	b.d.	b.d.	b.d.	b.d.	b.d.	b.d.	101.00
p68	b.d.	46.86	54.41	b.d.	b.d.	b.d.	b.d.	b.d.	b.d.	b.d.	b.d.	b.d.	101.30
p69	b.d.	46.81	54.02	b.d.	0.008	b.d.	0.02	0.08	b.d.	0.01	b.d.	b.d.	100.96
p70	b.d.	46.49	54.33	b.d.	b.d.	b.d.	b.d.	b.d.	b.d.	b.d.	b.d.	b.d.	100.87
p71	0.54	46.69	54.03	b.d.	b.d.	b.d.	b.d.	0.05	b.d.	b.d.	b.d.	b.d.	101.34
p72	b.d.	46.99	54.14	b.d.	b.d.	0.03	0.02	b.d.	0.02	b.d.	b.d.	b.d.	101.21
p73	0.80	45.50	53.78	b.d.	b.d.	b.d.	0.02	b.d.	b.d.	0.01	b.d.	b.d.	100.11
p74	b.d.	46.84	53.96	b.d.	b.d.	0.03	b.d.	b.d.	b.d.	0.01	b.d.	0.04	100.91
p75	b.d.	47.10	54.01	b.d.	0.02	0.02	b.d.	0.06	b.d.	0.01	b.d.	b.d.	101.23
p76	0.09	46.19	53.84	b.d.	b.d.	b.d.	0.01	b.d.	b.d.	b.d.	b.d.	b.d.	100.17
p77	b.d.	46.13	53.81	b.d.	0.03	b.d.	0.01	b.d.	b.d.	0.01	b.d.	b.d.	100.03
p78	b.d.	47.45	54.00	b.d.	b.d.	0.01	b.d.	b.d.	b.d.	0.02	0.006	b.d.	101.50
p79	b.d.	46.76	54.05	b.d.	0.02	0.01	b.d.	b.d.	b.d.	b.d.	b.d.	b.d.	100.89
p80	0.01	46.34	54.21	b.d.	0.02	0.01	b.d.	b.d.	b.d.	b.d.	b.d.	b.d.	100.63

Appendix 1C
Representative EMPA analyses (wt.%) of pyrite. b.d., below detection. Detection limits (wt.%) are shown below each element.

Sample PY-380	Cu (0.01)	Fe (0.30)	S (0.20)	As (0.01)	Co (0.008)	Ni (0.01)	Zn (0.013)	Hg (0.04)	Se (0.009)	Te (0.009)	Ag (0.006)	Au (0.04)	Total
p1	b.d.	46.31	53.13	0.59	b.d.	b.d.	b.d.	b.d.	b.d.	0.01	b.d.	b.d.	100.07
p2	b.d.	46.84	52.92	0.99	0.01	b.d.	b.d.	b.d.	b.d.	b.d.	b.d.	b.d.	100.80
p3	b.d.	47.07	53.79	b.d.	b.d.	b.d.	b.d.	b.d.	b.d.	b.d.	b.d.	b.d.	100.89
p4	b.d.	46.07	52.78	0.84	b.d.	b.d.	0.02	b.d.	b.d.	0.01	b.d.	b.d.	99.76
p5	b.d.	46.03	52.33	1.33	b.d.	b.d.	0.02	b.d.	b.d.	0.01	b.d.	b.d.	99.76
p6	b.d.	46.84	53.31	b.d.	b.d.	b.d.	0.014	0.04	b.d.	b.d.	b.d.	b.d.	100.22
p7	b.d.	46.42	52.41	1.31	b.d.	b.d.	0.015	b.d.	b.d.	b.d.	b.d.	b.d.	100.19
p8	b.d.	46.52	53.39	b.d.	0.016	b.d.	0.02	b.d.	b.d.	0.01	b.d.	b.d.	99.97
p9	b.d.	47.35	53.48	b.d.	0.008	b.d.	0.020	b.d.	b.d.	0.01	b.d.	b.d.	100.90
p10	b.d.	47.24	53.51	0.27	b.d.	b.d.	b.d.	0.05	b.d.	0.01	b.d.	b.d.	101.09
p11	b.d.	46.52	53.56	b.d.	b.d.	0.01	b.d.	b.d.	b.d.	b.d.	0.006	b.d.	100.12
p12	b.d.	46.93	53.97	b.d.	b.d.	b.d.	b.d.	b.d.	b.d.	b.d.	b.d.	b.d.	100.93
p13	b.d.	47.49	53.98	b.d.	b.d.	b.d.	b.d.	b.d.	0.009	b.d.	b.d.	0.04	101.57
p14	b.d.	46.39	52.37	1.40	b.d.	b.d.	b.d.	b.d.	0.015	b.d.	b.d.	0.07	100.26
p15	b.d.	46.73	53.56	b.d.	b.d.	b.d.	b.d.	0.08	b.d.	0.01	b.d.	b.d.	100.41
p16	b.d.	46.8	52.63	1.20	0.009	b.d.	b.d.	0.04	b.d.	b.d.	b.d.	b.d.	100.71
p17	b.d.	46.28	53.23	0.52	0.016	b.d.	b.d.	b.d.	b.d.	b.d.	b.d.	b.d.	100.08
p18	b.d.	46.03	52.95	0.86	b.d.	b.d.	200	b.d.	0.010	b.d.	b.d.	b.d.	99.93
p19	b.d.	46.81	52.80	0.88	0.011	b.d.	b.d.	b.d.	b.d.	b.d.	b.d.	b.d.	100.54
p20	b.d.	47.52	53.63	b.d.	b.d.	b.d.	b.d.	0.04	b.d.	0.02	b.d.	b.d.	101.21
p21	b.d.	47.16	53.63	b.d.	b.d.	b.d.	b.d.	b.d.	b.d.	b.d.	b.d.	b.d.	100.83
p22	b.d.	46.24	51.78	2.24	b.d.	b.d.	b.d.	0.12	b.d.	b.d.	b.d.	b.d.	100.41
p23	b.d.	45.78	51.50	2.45	0.009	b.d.	0.02	b.d.	b.d.	b.d.	b.d.	b.d.	99.77
p24	0.04	46.19	51.74	2.02	0.009	b.d.	b.d.	b.d.	0.015	b.d.	b.d.	b.d.	100.03
p25	0.02	45.63	51.45	2.58	0.012	b.d.	b.d.	b.d.	0.016	b.d.	b.d.	0.06	99.79
p26	3.32	43.73	53.15	b.d.	b.d.	b.d.	0.02	b.d.	b.d.	b.d.	0.008	b.d.	100.26
p27	b.d.	47.07	53.83	0.13	b.d.	b.d.	0.02	0.04	b.d.	b.d.	b.d.	b.d.	101.10
p28	b.d.	46.39	53.64	0.33	0.013	b.d.	0.02	b.d.	b.d.	b.d.	b.d.	b.d.	100.44
p29	b.d.	46.4	53.72	b.d.	b.d.	b.d.	0.014	b.d.	b.d.	b.d.	b.d.	b.d.	100.17
p30	b.d.	46.97	53.77	b.d.	0.013	b.d.	0.02	0.05	b.d.	b.d.	b.d.	b.d.	100.84
p31	0.04	46.04	51.67	2.51	b.d.	b.d.	0.03	b.d.	b.d.	b.d.	b.d.	b.d.	100.30
p32	b.d.	45.97	51.80	2.56	b.d.	b.d.	b.d.	b.d.	0.013	0.01	b.d.	0.06	100.43
p33	b.d.	46.26	51.57	2.38	0.012	b.d.	b.d.	b.d.	0.012	0.01	b.d.	b.d.	100.28
p34	b.d.	47.43	53.59	b.d.	b.d.	b.d.	b.d.	b.d.	b.d.	b.d.	b.d.	b.d.	101.04
p35	b.d.	47.15	53.82	0.01	b.d.	b.d.	b.d.	b.d.	b.d.	b.d.	b.d.	0.05	101.04

Appendix 1D
Representative EMPA analyses (wt.%) of pyrite. b.d., below detection. Detection limits (wt.%) are shown below each element.

Sample PY-550	Cu (0.01)	Fe (0.30)	S (0.20)	As (0.01)	Co (0.008)	Ni (0.01)	Zn (0.013)	Hg (0.04)	Se (0.009)	Te (0.009)	Ag (0.006)	Au (0.04)	Total
p1	b.d.	46.26	53.77	b.d.	0.01	b.d.	b.d.	b.d.	b.d.	0.02	0.01	b.d.	100.07
p2	b.d.	44.81	53.58	b.d.	b.d.	b.d.	0.02	b.d.	b.d.	0.01	b.d.	b.d.	98.48
p3	b.d.	45.69	53.60	b.d.	b.d.	0.01	b.d.	b.d.	b.d.	0.02	b.d.	b.d.	99.39
p4	b.d.	45.92	54.10	b.d.	0.01	0.02	b.d.	0.10	b.d.	0.01	b.d.	b.d.	100.17
p5	b.d.	45.71	53.85	b.d.	0.01	b.d.	0.02	b.d.	b.d.	b.d.	b.d.	b.d.	99.62
p6	b.d.	45.25	53.88	b.d.	0.01	b.d.	0.01	b.d.	b.d.	0.01	b.d.	0.04	99.21
p7	b.d.	46.03	53.73	b.d.	0.01	b.d.	b.d.	b.d.	b.d.	0.02	b.d.	b.d.	99.83
p8	b.d.	45.76	53.97	0.03	0.01	b.d.	0.01	0.07	b.d.	b.d.	b.d.	b.d.	99.85
p9	b.d.	45.77	53.98	b.d.	0.01	b.d.	0.02	b.d.	b.d.	0.01	b.d.	b.d.	99.82
p10	b.d.	45.63	53.62	b.d.	b.d.	b.d.	b.d.	b.d.	b.d.	b.d.	b.d.	b.d.	99.28
p11	b.d.	46.27	53.23	b.d.	0.01	b.d.	0.02	b.d.	b.d.	b.d.	b.d.	b.d.	99.56
p12	b.d.	45.61	53.83	b.d.	b.d.	0.01	0.02	b.d.	b.d.	b.d.	b.d.	0.04	99.54
p13	b.d.	45.22	53.81	b.d.	b.d.	b.d.	b.d.	0.04	b.d.	b.d.	b.d.	b.d.	99.09
p14	b.d.	45.83	53.72	0.01	b.d.	b.d.	0.01	b.d.	b.d.	0.01	b.d.	b.d.	99.62
p15	b.d.	46.14	53.77	0.01	0.01	0.01	0.02	b.d.	b.d.	0.01	b.d.	b.d.	100.02
p16	b.d.	45.46	53.85	b.d.	b.d.	b.d.	b.d.	0.06	b.d.	0.01	b.d.	b.d.	99.42
p17	b.d.	45.95	53.40	b.d.	0.02	0.01	b.d.	0.05	b.d.	0.02	b.d.	b.d.	99.45
p18	b.d.	45.72	53.87	b.d.	0.01	b.d.	0.02	b.d.	b.d.	b.d.	b.d.	b.d.	99.65
p19	b.d.	45.42	53.57	b.d.	0.01	b.d.	b.d.	b.d.	b.d.	b.d.	b.d.	b.d.	99.01
p20	b.d.	45.11	53.78	b.d.	b.d.	b.d.	0.01	b.d.	b.d.	0.05	b.d.	0.25	99.25
o21	b.d.	46.03	53.49	b.d.	0.01	b.d.	0.01	b.d.	b.d.	b.d.	b.d.	0.04	99.63
o22	b.d.	46.31	53.46	b.d.	0.01	b.d.	b.d.	0.06	b.d.	b.d.	b.d.	b.d.	99.87
o23	b.d.	45.98	53.46	b.d.	b.d.	b.d.	0.02	b.d.	b.d.	b.d.	b.d.	b.d.	99.54
o24	b.d.	46.19	53.54	b.d.	b.d.	0.03	0.02	b.d.	b.d.	b.d.	b.d.	b.d.	99.81
o25	b.d.	46.31	53.47	b.d.	0.01	b.d.	b.d.	0.05	b.d.	0.01	b.d.	b.d.	99.86
o26	b.d.	46.19	53.03	b.d.	0.02	0.02	b.d.	b.d.	0.01	b.d.	b.d.	b.d.	99.33
o27	b.d.	46.16	53.81	b.d.	b.d.	0.01	0.01	b.d.	b.d.	0.02	b.d.	b.d.	100.10
o28	b.d.	46.34	53.30	0.03	b.d.	b.d.	b.d.	b.d.	b.d.	b.d.	b.d.	b.d.	99.72
o29	b.d.	46.75	52.69	b.d.	0.01	b.d.	b.d.	0.06	b.d.	0.01	b.d.	b.d.	99.53
o30	b.d.	46.46	53.39	b.d.	0.02	0.01	b.d.	0.08	b.d.	b.d.	b.d.	b.d.	99.97
o31	b.d.	46.92	53.58	0.04	0.01	0.01	b.d.	b.d.	b.d.	b.d.	b.d.	b.d.	100.63
o32	b.d.	46.61	53.44	b.d.	b.d.	0.02	b.d.	0.10	0.01	0.01	b.d.	b.d.	100.22
o33	b.d.	46.44	53.21	b.d.	b.d.	b.d.	b.d.	b.d.	b.d.	b.d.	b.d.	b.d.	99.68
o34	b.d.	45.87	53.07	b.d.	b.d.	b.d.	0.01	b.d.	b.d.	0.01	b.d.	b.d.	99.01
o35	b.d.	46.73	53.11	b.d.	0.01	b.d.	b.d.	b.d.	b.d.	0.01	b.d.	b.d.	99.91
o36	b.d.	46.86	53.52	b.d.	b.d.	b.d.	b.d.	b.d.	b.d.	0.02	b.d.	0.08	100.51
o37	b.d.	46.73	53.38	b.d.	b.d.	b.d.	0.01	b.d.	b.d.	0.01	b.d.	b.d.	100.15
o38	b.d.	46.22	53.67	b.d.	0.01	b.d.	0.01	b.d.	b.d.	b.d.	b.d.	b.d.	99.94
o39	b.d.	45.97	53.06	b.d.	0.02	0.02	b.d.	0.11	b.d.	b.d.	b.d.	b.d.	99.19
o40	b.d.	46.08	53.63	b.d.	b.d.	b.d.	b.d.	b.d.	b.d.	0.01	b.d.	b.d.	99.77

Appendix 1E
Representative EMPA analyses (wt.%) of pyrite. b.d., below detection. Detection limits (wt.%) are shown below each element.

Sample PY-800	Cu (0.01)	Fe (0.30)	S (0.20)	As (0.01)	Co (0.008)	Ni (0.01)	Zn (0.013)	Hg (0.04)	Se (0.009)	Te (0.009)	Ag (0.006)	Au (0.04)	Total
p81	b.d.	46.82	54.35	b.d.	b.d.	0.01	0.02	b.d.	b.d.	b.d.	0.01	b.d.	101.21
p82	b.d.	46.56	53.95	b.d.	0.01	0.01	b.d.	0.04	b.d.	0.01	b.d.	b.d.	100.59
p83	b.d.	46.87	54.17	b.d.	b.d.	b.d.	0.01	b.d.	b.d.	0.01	b.d.	b.d.	101.12
p84	b.d.	46.5	54.22	0.01	b.d.	0.01	b.d.	0.06	b.d.	0.01	b.d.	0.05	100.89
p85	b.d.	46.94	53.84	b.d.	b.d.	b.d.	0.01	b.d.	b.d.	0.01	b.d.	0.04	100.89
p86	b.d.	46.54	54.09	b.d.	b.d.	b.d.	0.01	0.05	b.d.	b.d.	b.d.	b.d.	100.71
p87	b.d.	46.38	54.12	b.d.	0.02	0.02	0.01	0.04	b.d.	b.d.	b.d.	b.d.	100.63
p88	b.d.	47.1	54.29	b.d.	0.01	0.02	b.d.	0.05	b.d.	0.02	b.d.	0.05	101.53
p89	b.d.	46.89	54.30	b.d.	0.01	b.d.	b.d.	0.08	0.01	0.01	b.d.	b.d.	101.31
p90	b.d.	46.07	53.87	b.d.	b.d.	b.d.	b.d.	b.d.	b.d.	b.d.	b.d.	b.d.	99.95
p91	b.d.	45.91	54.31	b.d.	b.d.	b.d.	b.d.	b.d.	b.d.	b.d.	b.d.	0.05	100.30
p92	b.d.	47.12	53.91	b.d.	0.01	b.d.	b.d.	b.d.	b.d.	b.d.	b.d.	b.d.	101.08
p93	0.03	46.06	54.14	b.d.	0.02	b.d.	b.d.	0.06	b.d.	b.d.	b.d.	b.d.	100.33
p94	b.d.	46.05	53.92	b.d.	0.04	b.d.	b.d.	0.04	b.d.	0.01	b.d.	b.d.	100.09
p95	b.d.	47.29	54.04	b.d.	0.01	0.01	b.d.	b.d.	b.d.	b.d.	b.d.	b.d.	101.39
p96	b.d.	46.9	54.10	b.d.	0.03	0.09	b.d.	b.d.	0.01	b.d.	b.d.	b.d.	101.17
p97	b.d.	45.81	54.10	b.d.	0.01	b.d.	b.d.	b.d.	b.d.	b.d.	b.d.	b.d.	99.94
p98	b.d.	45.88	54.27	b.d.	b.d.	0.04	b.d.	0.05	0.01	b.d.	b.d.	b.d.	100.26
p99	b.d.	46.71	53.90	b.d.	b.d.	0.03	b.d.	0.04	b.d.	b.d.	b.d.	b.d.	100.70
p100	b.d.	46.58	54.33	b.d.	0.01	0.03	0.01	0.07	b.d.	b.d.	b.d.	b.d.	101.04
p101	b.d.	45.53	54.49	b.d.	0.07	0.02	b.d.	b.d.	b.d.	b.d.	b.d.	0.06	100.18
p102	b.d.	46.07	54.40	b.d.	0.02	0.02	b.d.	b.d.	b.d.	b.d.	b.d.	b.d.	100.53
p103	b.d.	46.83	54.18	b.d.	b.d.	0.02	b.d.	b.d.	b.d.	0.01	b.d.	0.04	101.09
p104	b.d.	46.31	54.19	b.d.	0.03	b.d.	0.01	0.07	b.d.	b.d.	b.d.	b.d.	100.62
p105	b.d.	45.7	54.20	b.d.	0.08	0.01	0.01	b.d.	b.d.	b.d.	b.d.	b.d.	100.02
p106	b.d.	46.87	54.18	b.d.	0.01	0.01	b.d.	b.d.	b.d.	0.02	b.d.	b.d.	101.13
p107	b.d.	46.12	53.72	0.19	0.01	0.01	b.d.	0.05	b.d.	b.d.	b.d.	b.d.	100.12
p108	b.d.	46.1	54.19	b.d.	b.d.	b.d.	b.d.	b.d.	b.d.	b.d.	b.d.	b.d.	100.30
p109	b.d.	46.47	54.21	b.d.	0.14	b.d.	b.d.	b.d.	b.d.	0.01	b.d.	0.05	100.95
p110	b.d.	46.96	53.90	b.d.	b.d.	b.d.	b.d.	b.d.	b.d.	0.02	b.d.	b.d.	100.89

Appendix 2
Secondary ion mass spectrometry (SIMS) analyses of Au, Ag, Cu, As, Sb, Se, Te and Co in pyrite from the Dexing deposit, China.

Sample	Au (ppm)	Ag (ppm)	Cu (ppm)	As (ppm)	Sb (ppm)	Co (ppm)	Se (ppm)	Te (ppm)
PY-190	0.07	n.d.	4.4	3.07	n.d.	3.4	2.1	0.27
	0.06	n.d.	198	n.d.	0.20	53	11.1	0.52
	0.17	n.d.	26	9.87	n.d.	2.2	3.4	0.17
	0.12	3.97	1.6	0.18	3.70	28	19.3	0.9
	0.05	n.d.	17.5	n.d.	n.d.	77	6.8	0.20
	0.04	n.d.	1.5	0.51	1.02	3.6	3.1	6.10
	0.36	n.d.	5.2	8.46	n.d.	3.4	2	1.25
	0.01	n.d.	3.4	0.20	n.d.	167	50	0.27
	n.d.	n.d.	3.4	n.d.	n.d.	1.3	2.2	0.20
	0.02	n.d.	4.6	0.49	0.02	1.3	1.2	0.45
	0.55	n.d.	5.6	65	n.d.	5.1	0.8	16.5
	0.04	n.d.	19.8	n.d.	n.d.	70	3.2	0.35
	0.02	n.d.	175	18.28	n.d.	0.2	3.9	3.45
	0.04	n.d.	5.8	4.87	n.d.	0.7	1.2	3.40
	0.08	n.d.	98	0.08	n.d.	3.3	2.4	0.60
	0.51	n.d.	4427	315	n.d.	1.24	27.8	0.62
	1.23	8.6	1177	16.8	20.3	21.8	13.1	27.4
	1.76	4.8	4304[a]	1.3	n.d.	0.14	3.82	1.25
	1.48	23.6	129	41.8	25.3	6.91	39.9	35.4
	1.64	3.3	54	121	14.8	7.59	8.88	21.4
	1.04	6.7	1504	4.5	22.9	6.09	3.96	68.7
	4.05[a]	48.5	5505	21.9	46.2	0.40	1.74	15.5
	0.91	4.7	849	9.0	6.8	11.3	2.74	10.5
	1.90	12.4	5558	0.4	n.d.	0.01	9.82	1.90
	1.44	17.7	1792	2.9	12.5	2.79	9.48	19.4
	10.8[a]	43.9	15980	45	29.9	3.56	2.68	37.7
	1.28	9.9	2956	2.9	1.2	9.89	6.14	3.67
	0.93	n.d.	1847	24	14.1	16.2	1.73	8.40
	1.84	10.4	2969	19	5.1	0.21	1.74	8.57
PY-270	0.02	0.77	30	n.d.	n.d.	16.7	2.37	n.d.
	0.08	n.d.	24	n.d.	4.47	1.5	0.80	0.25
	0.19	2.87	0.1	n.d.	2.00	129	15.9	0.27
	0.14	n.d.	10.6	n.d.	6.02	0.2	0.27	1.35
	0.25	2.37	1351[a]	1223	17.9	n.d.	n.d.	0.34
	0.18	n.d.	1379	1613	11.4	0.3	n.d.	0.32
	0.23	n.d.	42	n.d.	2.82	0.7	0.78	2.85
	0.07	n.d.	0.3	n.d.	n.d.	7.7	3.76	0.32
	0.16	3.50	1105	18	4.75	0.2	0.02	6.55
	0.02	n.d.	1046	5.6	n.d.	0.4	13.3	4.17
	0.11	2.25	937	0.3	n.d.	4.2	2.02	1.65
	n.d.	n.d.	48	n.d.	n.d.	n.d.	0.38	0.27
	0.13	n.d.	15	17.4	2.30	20	2.76	6.10
	0.12	n.d.	0.3	n.d.	2.92	n.d.	n.d.	0.50
	n.d.	n.d.	n.d.	2.6	n.d.	10	4.60	n.d.
	0.09	n.d.	23	n.d.	n.d.	1.3	4.77	n.d.
	0.02	n.d.	757	n.d.	n.d.	139	13.0	2.87
	0.01	n.d.	n.d.	1.7	1.50	168	57.2	0.47
	0.22	3.30	4.6	n.d.	1.50	1.0	3.41	1.42
	0.10	n.d.	1.3	n.d.	n.d.	58	0.76	0.27
	0.04	n.d.	17	n.d.	n.d.	17.8	1.91	0.87
	0.12	n.d.	26	n.d.	0.12	8.6	2.24	1.52
	0.09	0.82	51	n.d.	n.d.	3.7	4.55	0.26
PY-380	0.02	n.d.	7.1	6.0	n.d.	0.5	0.17	n.d.
	0.03	n.d.	8.4	15.5	n.d.	0.3	0.29	0.27
	0.02	n.d.	11.6	185	0.25	2.8	1.51	0.5
	0.02	n.d.	314	30	2.20	1.6	3.42	1.07
	0.01	n.d.	11.7	6.5	n.d.	2.4	2.56	0.25
	0.04	n.d.	177	107	n.d.	0.1	0.07	0.65
	n.d.	n.d.	2.6	n.d.	n.d.	n.d.	0.14	n.d.
	0.28	n.d.	153	114	2.17	n.d.	0.73	3.27
	0.12	n.d.	9.6	68	0.35	0.1	0.26	3.87
	0.06	n.d.	13.4	0.3	n.d.	1.3	1.12	0.22
	0.08	n.d.	6.1	1.5	1.35	0.1	0.48	3.40
	0.02	n.d.	18.6	n.d.	0.50	17	4.57	0.32
	0.04	n.d.	10.6	18	n.d.	0.2	0.25	0.10
	0.02	n.d.	0.7	1.1	n.d.	24	3.44	n.d.
	0.01	n.d.	2.7	n.d.	n.d.	82	5.66	n.d.
	n.d.	n.d.	14.2	n.d.	1.00	0.4	0.47	0.15
	0.38	2.85	158	441	4.87	1.3	1.83	2.52
	n.d.	n.d.	1.8	12.8	n.d.	2.7	0.91	0.10
	n.d.	n.d.	1.0	n.d.	n.d.	34	10.8	0.12
	0.66	2.20	67	958	n.d.	n.d.	0.28	4.87

(*continued on next page*)

Appendix 2 (*continued*)

Sample	Au (ppm)	Ag (ppm)	Cu (ppm)	As (ppm)	Sb (ppm)	Co (ppm)	Se (ppm)	Te (ppm)
PY-550	0.04	n.d.	4.9	117	n.d.	6.7	6.5	0.60
	n.d.	n.d.	11	1.89	n.d.	10	10.7	0.07
	0.01	n.d.	3.2	0.46	n.d.	0.2	1.9	0.30
	0.05	n.d.	5.9	38.2	n.d.	8.2	4.0	0.42
	0.12	n.d.	17.4	61.1	n.d.	6.2	3.20	0.77
	0.07	2.20	15.9	2.06	n.d.	10	4.0	0.87
	n.d.	1.65	2.9	6.92	n.d.	72	67.7	0.45
	0.18	3.32	2.7	3.00	16.4	n.d.	8.6	0.10
	0.02	0.87	2.1	0.32	n.d.	n.d.	1.3	0.02
	0.10	3.20	16.7	26.3	n.d.	6.8	10.2	0.17
	0.12	12.9	11.6	1.04	7.77	n.d.	0.3	0.80
	0.19	n.d.	4.9	0.65	13.6	33	6.2	0.57
	0.03	n.d.	6.3	164	n.d.	3.5	2.4	0.30
	0.12	6.87	11.6	9.08	n.d.	5.8	3.1	1.62
	0.08	n.d.	6.1	44.9	n.d.	12.5	10.4	0.25
	0.11	n.d.	14.9	6.58	5.67	n.d.	1.4	0.27
	0.04	n.d.	7.5	0.32	n.d.	1.4	5.5	0.02
	n.d.	n.d.	46.3	13.3	n.d.	11.3	6.0	0.70
	0.01	n.d.	31.0	60.5	1.87	2.7	1.30	1.17
	0.15	3.12	24.4	12.3	25.2	4.2	2.59	3.07
	0.18	n.d.	65.2	74.0	3.25	14.3	6.94	9.57
	0.59	3.65	26.7	26.5	7.20	19.1	4.42	7.45
	0.16	n.d.	142	76.2	11.4	48.7	1.22	3.4
	n.d.	n.d.	12.7	17.3	1.87	22.2	1.27	3.05
	0.16	n.d.	114	79.0	30.9	100	1.96	14.4
	0.15	n.d.	35.0	38.0	9.62	26.6	1.42	8.15
	0.13	n.d.	30.2	117	2.35	11.2	0.60	0.82
	0.39	2.25	49.8	114	9.07	10.5	1.45	3.12
	0.13	11.3	54.9	61.8	26.1	43.4	0.62	17.4
	0.11	0.17	14.3	23.5	9.50	21.3	2.52	4.07
	0.29	8.12	114.	60.8	13.1	28.4	0.73	7.97
	0.11	0.35	42.1	10.1	7.70	17.7	5.22	5.57
	0.46	13.1	155	65.4	23.4	29.3	0.98	8.62
	n.d.	n.d.	23.4	5.50	n.d.	7.8	2.42	6.95
	0.23	1.02	50.1	138	5.30	10.2	1.45	3.50
PY-800	0.05	n.d.	14	10	3.57	67.1	7.88	2.20
	0.12	2.60	2.9	637	4.70	32.2	2.43	4.50
	0.04	n.d.	0.8	0.6	n.d.	57	6.2	0.02
	0.30	n.d.	10.6	7.8	2.57	126	19.6	5.00
	0.07	n.d.	0.6	15	15.8	221	26.2	28.7
	0.19	12.4	9.3	19	12.1	119	10.7	12.3
	0.10	n.d.	7.6	23.5	n.d.	8.1	22.0	1.15
	0.02	n.d.	1.0	1.3	n.d.	4.0	27.1	0.05
	0.01	n.d.	16	4.5	7.70	2.3	23.1	11.47
	n.d.	n.d.	0.8	n.d.	n.d.	0.4	7.2	0.07
	0.36	n.d.	n.d.	n.d.	n.d.	11.7	2.99	0.17
	0.05	n.d.	0.3	n.d.	n.d.	15.3	3.67	n.d.
	0.08	n.d.	17	n.d.	0.27	3.6	15.9	1.07
	0.08	n.d.	305	3.8	0.72	0.2	3.35	0.52
	0.15	0.50	7.6	1.4	2.80	1.5	0.05	5.47
	0.08	n.d.	n.d.	n.d.	n.d.	22.0	7.47	0.05
	n.d.	n.d.	0.4	2.4	n.d.	1.3	15.0	0.95
	0.08	n.d.	11.2	5.0	n.d.	0.8	1.22	15.2
	n.d.	n.d.	n.d.	n.d.	n.d.	142	10.7	0.05
	0.04	n.d.	1.6	2.1	n.d.	0.7	2.05	4.55
	n.d.	n.d.	0.9	n.d.	n.d.	13.5	13.1	n.d.
	0.08	n.d.	2.0	16.0	n.d.	54.1	2.75	0.70

[a] Samples (and elements) that were depth-profiled using SIMS.

Finally, it is important to note that the presence of relatively high amounts of Ni (<2000 ppm) in pyrite at Dexing suggests the influence of a mafic source or Ni-leaching from wall-rocks and its subsequent redistribution. The occur-

rence of Ni-rich growth zones in Pyrite-I cores, as seen in Fig. 4F, is evidence of compositional variations in the fluid phase during the early phases of pyrite growth, before introduction of Cu, As and Au. This is consistent with recent observations by Hanley et al. (2010) that documented enrichment in Ni (and Co) in pyrites from alkalic porphyry deposits within the Canadian Cordillera during an early, high-temperature hydrothermal event that pre-dated Cu and Au deposition. As noted by Hanley et al. (2010), Ni-rich pyrite is an important repository of platinum-group elements (PGE), and PGE incorporation into pyrite coincided with Ni and Co enrichment during this early hydrothermal stage.

Despite the fact that more studies are needed to increase our knowledge about metal partitioning in sulfides during the hydrothermal stages of porphyry emplacement and deposit formation, the observations and data presented here support an important role of pyrite as a record of fluid variations, and an important host of metalloids (As), precious (Au) and base (Cu) metal, and potentially PGEs.

5. CONCLUSIONS

The first comprehensive EMPA–SIMS database of trace metal contents in pyrite from a porphyry Cu system reveals that significant concentrations of base and heavy metals (e.g., Cu, Ni, Hg), precious metals (e.g., Au, Ag) and metalloids (e.g., As, Te, Sb) can be hosted in this abundant and ubiquitous mineral phase. EMPA–WDS elemental mapping and SIMS depth profiling revealed that some of these metals occur exclusively in solid solution in the pyrite structure (e.g., As, Ni) or are present in solid solution and also in micro- to nano-sized inclusions of chalcopyrite and native Au. These mineralogical occurrences are strongly associated to complex textural and chemical features, such as oscillatory growth zoning and sector zoning with variable porosity, where Cu-rich, As-(precious metals)-poor zones alternate with As-(precious metals rich)-rich, Cu-poor zones, and with barren pyrite zones where trace element concentrations are below 10–100 ppm. These observations point toward a decoupled behavior of Cu and As in this porphyry system, strongly suggesting that selective partitioning of metals into pyrite is most likely the result of changes in fluid composition, probably caused by fluid mixing and repeated and intermittent pulses of Cu and As-bearing fluids of magmatic/hydrothermal origin (Audétat et al., 1998; Heinrich et al., 1999, 2004). Considering the fact that pyrite is ubiquitous and abundant in porphyry Cu deposits and that mineralized veins represent the main locus of fluid flux (Seedorff et al., 2005), we conclude that pyrite may play a significant role as a scavenger of metals and monitor of fluid changes in hydrothermal systems.

ACKNOWLEDGMENTS

The authors would like to acknowledge support received from FONDECYT grant no. 11070088 to Martin Reich, and additional support from FONDAP project no. 15090013 “Centro de Excelencia en Geotermia de los Andes, CEGA”. We thank Uwe Reimold (Associate Editor), Hartwig Frimmel, and two anonymous reviewers for their constructive reviews of the manuscript.

APPENDIX

See Appendix 1A–E and 2

REFERENCES

Arehart G. B., Chryssoulis S. L. and Kesler S. E. (1993) Gold and arsenic in iron sulfides from sediment-hosted disseminated gold deposits; implications for depositional processes. *Econ. Geol.* **88**, 171–185.

Audétat A., Günther D. and Heinrich C. A. (1998) Formation of a magmatic–hydrothermal ore deposit: insights with LA-ICP-MS analysis of fluid inclusions. *Science* **279**, 2091–2094.

Audétat A., Pettke T., Heinrich C. A. and Bodnar R. J. (2008) The composition of magmatic-hydrothermal fluids in barren and mineralized intrusions. *Econ. Geol.* **103**, 1–32.

Barker S. L. L., Hickey K. A., Cline J. S., Dipple G. M., Kilburn M. R., Vaughan J. R. and Anthony Longo A. A. (2009) Uncloaking invisible gold: use of NanoSIMS to evaluate gold, trace elements, and sulfur isotopes in pyrite from Carlin-type gold deposits. *Econ. Geol.* **104**, 897–904.

Bayliss P. (1989) Crystal chemistry and crystallography of some minerals within the pyrite group. *Am. Mineral.* **74**, 1168–1176.

Beane R. E. (1982) Hydrothermal alteration in silicate rocks, southwestern North America. In *Advances in Geology of Porphyry Copper Deposits; Southwestern North America* (ed. S. R. Titley). University of Arizona Press, Tucson, pp. 117–137.

Beane R. E. and Bodnar R. J. (1995) Hydrothermal fluids and hydrothermal alteration in porphyry copper deposits. In *Porphyry Copper Deposits of the American Cordillera* (eds. F.W. Pierce and J. G. Bohm). *Arizona Geological Society Digest* **20**, 83–93.

Benzaazoua M., Marion P., Robaut F. and Pinto A. (2007) Gold-bearing arsenopyrite and pyrite in refractory ores: analytical refinements and new understanding of gold mineralogy. *Mineral. Mag.* **71**, 123–142.

Campbell F. A. and Ethier V. G. (1984) Nickel and cobalt in pyrrhotite and pyrite from the Faro and Sullivan orebodies. *Can. Mineral.* **22**, 503–506.

Candela P. A. and Holland H. D. (1984) The partitioning of copper and molybdenum between silicate melts and aqueous fluids. *Geochim. Cosmochim. Acta* **48**, 373–380.

Chryssoulis S. (1990) Detection and quantification of “invisible” gold by microprobe techniques. In *Proc. Symp. Gold 90', Soc. for Mining, Metall., and Explor.* (eds. D. M. Hausen, D. N. Halbe, E. U. Petersen and W. J. Tafuri). Littleton, pp. 323–331.

Chryssoulis S. L., Dunne R. and Coetzee A. (2004) Diagnostic microbeam technology in gold ore processing. *J. Min. Metall. Mater. Soc.* **56**, 53–57.

Ciobanu C. L., Cook N. J., Pring A., Brugger J., Danyushevsky L. V. and Shimizu M. (2009) “Invisible gold” in bismuth chalcogenides. *Geochim. Cosmochim. Acta* **73**, 1970–1999.

Clark A. H. (1970) Copper zoning in pyrite from Cerro de Pasco, Perú: further discussion. *Am. Mineral.* **55**, 525–527.

Cline J. S. (2001) Timing of gold and arsenic sulfide mineral deposition at the Getchell Carlin-type gold deposit, north-central Nevada. *Econ. Geol.* **96**, 75–89.

Cline J. S., Hofstra A. H., Muntean J. L., Tosdal R. M. and Hickey K. A. (2005) Carlin-type gold deposits in Nevada: critical geologic characteristics and viable models. *Econ. Geol.* **100th Anniversary Volume**, 451–454.

Cook N. J. and Chryssoulis S. L. (1990) Concentrations of invisible gold in the common sulfides. *Can. Mineral.* **28**, 1–16.

Cook N. J., Ciobanu C. L. and Mao J. (2009a) Textural control on gold distribution in As-free pyrite from the Dongping, Huangtuliang and Hougou gold deposits, North China Craton (Hebei Province, China). *Chem. Geol.* **264**, 101–121.

Cook N. J., Ciobanu C. L., Pring A., Skinner W., Shimizu M., Danyushevsky L. V., Saini-Eldukat B. and Melcher F. (2009b) Trace and minor elements in sphalerite: a LA-ICP-MS study. *Geochim. Cosmochim. Acta* **73**, 4761–4791.

Cook N. J., Ciobanu C. L., Danyushevsky L. V. and Gilbert S. (2011) Minor and trace elements in bornite and associated Cu–(Fe) sulfides: a LA-ICP-MS study. *Geochim. Cosmochim. Acta* **75**, 6473–6496.

Deditius A., Utsunomiya S., Renock D., Ewing R. C., Ramana C. V., Becker U. and Kesler S. E. (2008) A proposed new type of arsenian pyrite: composition, nanostructure and geochemical sgnificance. *Geochim. Cosmochim. Acta* **72**, 2919–2933.

Deditius A. P., Utsunomiya S., Ewing R. C. and Kesler S. E. (2009a) Nanoscale "liquid" inclusions of As–Fe–S in arsenian pyrite. *Am. Mineral.* **94**, 391–394.

Deditius A., Utsunomiya S., Ewing R. C., Chryssoulis S. L., Venter D. and Kesler S. E. (2009b) Decoupled geochemical behavior of As and Cu in hydrothermal systems. *Geology* **37**, 707–710.

Deditius A., Utsunomiya S., Reich M., Kesler S. E., Ewing R. C., Hough R. and Walshe J. (2011) Trace metal nanoparticles in pyrite. *Ore Geol. Rev.* **42**, 32–46.

Einaudi M. T. (1968) Copper zoning in pyrite from Cerro de Pasco, Perú. *Am. Mineral.* **53**, 1748–1752.

Emsbo P., Hofstra A. H., Lauha E. A., Griffin G. L., Hutchinson R. W., John D. A. and Theodore T. G. (2003) Origin of high-grade gold ore, source of ore fluid components, and genesis of the Meikle and neighboring Carlin-type deposits, northern Carlin Trend, Nevada. *Econ. Geol.* **98**, 1069–1105.

Fleet M. E., Chryssoulis S. L., MacLean P. J., Davidson R. and Weisener C. G. (1993) Arsenian pyrite from gold deposits; Au and As distribution investigated by SIMS and EMP, and color staining and surface oxidation by XPS and LIMS. *Can. Mineral.* **31**, 1–17.

Frenzel G. and Ottemann J. (1967) Eine sulfidparagenese mit kupferhaltigem Zonar-pyrit von Nukundamu/Fiji. *Mineral. Deposita* **l**, 307–316.

Gustafson L. B. and Hunt J. P. (1975) The porphyry copper deposit at El Salvador, Chile. *Econ. Geol.* **70**, 857–912.

Gustafson L. B. and Quiroga G. J. (1995) Patterns of mineralization and alteration below the porphyry copper orebody at El Salvador, Chile. *Econ. Geol.* **90**, 2–16.

Hanley J. J. and MacKenzie M. K. (2009) Incorporation of platinum-group elements and cobalt into subsidiary pyrite in alkalic Cu–Au porphyry deposits: significant implications for precious metal distribution in felsic magmatic-hydrothermal systems. In *American Geophysical Union, Spring Meeting 2009*, V14A-03.

Hanley J. J., MacKenzie M. K., Warren M. R., and Guillong M. (2010) Distribution and origin of platinum-group elements in alkalic porphyry Cu–Au and low sulfidation epithermal Au deposits in the Canadian Cordillera. In *11th International Platinum Symposium*, June 21–24.

Hannington M. D., Poulsen K. H., Thompson J. F. H. and Sillitoe R. (1999) Volcanogenic gold in the massive sulfide environment. *Rev. Econ. Geol.* **8**, 325–356.

Harris A. C. and Golding S. D. (2002) New evidence of magmatic-fluid-related phyllic alteration: implications for the genesis of porphyry Cu deposits. *Geology* **30**, 335–338.

Heinrich C. A. (2007) Fluid – fluid interactions in hydrothermal ore formation. *Reviews in Mineralogy and Geochemistry* **65**, 363–387.

Heinrich C. A., Gunther D., Audétat A., Ulrich T. and Frischknecht R. (1999) Metal fractionation between magmatic brine and vapour, determined by microanalysis of fluid inclusions. *Geology* **27**, 755–758.

Heinrich C. A., Driesner T., Stefánsson A. and Seward T. M. (2004) Magmatic vapour contraction and the transport of gold from porphyry environment to epithermal ore deposits. *Geology* **32**, 761–764.

Heinrich C. A., Halter W. E. and Pettke T. (2005) The formation of economic porphyry copper (gold) deposits: constraints from microanalysis of fluid and melt inclusions. In *Mineral Deposits and Earth Evolution* (ed. I. McDonald, et al.). *Geol. Soc. (London) Spec. Publ.* **248**, 247–263.

Hochella M. F., Moore J. N., Golla U. and Putnis A. (1999) TEM study of samples from acid mine drainage systems: metal–mineral association with implications for transport. *Geochim. Cosmochim. Acta* **63**, 3395–3406.

Hough R. M., Noble R. R. P., Hitchen G. J., Hart R., Reddy S. M., Saunders M., Clode P., Vaughan D., Lowe J., Gray D. J., Anand R. R., Butt C. R. M. and Verral M. (2008) Naturally occurring gold nanoparticles and nanoplates. *Geology* **36**, 571–574.

Huston D. L., Sie S. H., Suter G. F., Cooke D. R. and Both R. A. (1995) Trace elements in sulfide minerals from eastern Australian volcanic-hosted massive sulfide deposits: Part I, proton microprobe analyses of pyrite, chalcopyrite, and sphalerite, and Part II, selenium levels in pyrite: comparison with δ34S values and implications for the source of sulfur in volcanogenic hydrothermal systems. *Econ. Geol.* **90**, 1167–1196.

John E. C. (1978) Mineral zones in the Utah Copper orebody. *Econ. Geol.* **73**, 1250–1259.

Kaneda H., Shimazaki H. and Lee M. S. (1986) Mineralogy and geochemistry of the Au–Ag ore deposits of the South Korean Peninsula. *Mineral. Deposita* **21**, 234–243.

Kerrich R., Goldfarb R., Groves D. and Garwin S. (2000) The geodynamics of world-class gold deposits: characteristics, space-time distributions, and origins. *Rev. Econ. Geol.* **13**, 501–551.

Kesler S. E., Chryssoulis S. L. and Simon G. (2002) Gold in porphyry copper deposits: its abundance and fate. *Ore Geol. Rev.* **21**, 103–124.

Klemm L. M., Pettke T., Heinrich C. A. and Campos E. (2007) Hydrothermal evolution of the El Teniente deposit, Chile: porphyry Cu–Mo ore deposition from low-salinity magmatic fluids. *Econ. Geol.* **102**, 1021–1045.

Koglin N., Frimmel H. E., Lawrie Minter W. E. and Brätz H. (2010) Trace-element characteristics of different pyrite types in Mesoarchean to Palaeoproterozoic placer deposits. *Mineral. Deposita* **45**, 259–280.

Kouzmanov K., Pettke T. and Heinrich C. A. (2010) Direct analysis of ore-precipitating fluids: combined IR microscopy and LA-ICP-MS study of fluid inclusions in opaque ore minerals. *Econ. Geol.* **105**, 351–373.

Large D. J., Sawlowicz Z. and Spratt J. (1999) A cobaltite–framboidal pyrite association from the Kupferschiefer; possible implications for trace element behaviour during the earliest stages of diagenesis. *Mineral. Mag.* **63**, 353–361.

Large R. R., Danyushevsky L. V., Hollit C., Maslennikov V., Meffre S., Gilbert S. E., Bull S., Scott R. J., Emsbo P., Thomas H., Singh B. and Foster J. (2009) Gold and trace element zonation in pyrite using a laser imaging technique: implications for the timing of gold in orogenic and Carlin-style sediment-hosted deposits. *Econ. Geol.* **104**, 635–668.

Li X. and Sasaki M. (2007) Hydrothermal alteration and mineralization of middle Jurassic dexing porphyry Cu–Mo deposit, southeast China. *Resour. Geol.* **57**, 409–426.

Lowell J. D. and Guilbert J. M. (1970) Lateral and vertical alteration–mineralization zoning in porphyry ore deposits. *Econ. Geol.* **65**, 373–408.

Mao J., Zhang J., Pirajno F., Ishiyama D., Su H., Guo C. and Chen Y. (2011) Porphyry Cu–Au–Mo–epithermal Ag–Pb–Zn–distal hydrothermal Au deposits in the Dexing area, Jiangxi province, East China – a linked ore system. *Ore Geol. Rev.* **43**, 203–216.

Matlock M. M., Howerton B. S. and Atwood D. A. (2002) Chemical precipitation of heavy metals from acid mine drainage. *Water Res.* **36**, 4757–4764.

Morey A. A., Tomkins A. G., Bierlin F. P., Wienberg R. F. and Davidson G. J. (2008) Bimodal distribution of gold in pyrite and arsenopyrite: examples from the Archean Boorara and Bardoc shear systems, Yilgarn craton, Western Australia. *Econ. Geol.* **103**, 599–614.

Muntean J. L., Cline J. S., Simon A. C. and Longo A. A. (2011) Magmatic–hydrothermal origin of Nevada's Carlin-type gold deposits. *Nat. Geosci.* **4**, 122–127.

Nielsen R. L. (1968) Hypogene texture and mineral zoning in a copper-bearing granodiorite stock, Santa Rita, New Mexico. *Econ. Geol.* **63**, 37–50.

Palenik C. S., Utsunomiya S., Reich M., Kesler S. E. and Ewing R. C. (2004) "Invisible" gold revealed: direct imaging of gold nanoparticles in a Carlin-type deposit. *Am. Mineral.* **89**, 1359–1366.

Pacevski A., Libowitzky E., Zivkovic P., Dimitrijevic R. and Cvetkovic L. (2008) Copper-bearing pyrite from the Coka Marin polymetallic deposit, Serbia: mineral inclusions or true solid-solution? *Can. Mineral.* **46**, 249–261.

Pasava J., Vymazalova A., Kosler J., Koneev R., Jukov A. V. and Khalmatov R. A. (2010) Platinum-group elements in ores from the Kalmakyr porphyry Cu–Au–Mo deposit, Uzbekistan: bulk geochemical and laser ablation ICP-MS data. *Miner. Deposita* **45**, 411–418.

Pirajno F. (2009) *Hydrothermal Processes and Mineral Systems*. Springer Science, 1250 pp..

Pokrovski G. S., Zakirov I. V., Roux J., Testemale D., Hazemann J. L., Bychkov A. V. and Golikova G. V. (2002) Experimental study of arsenic speciation in vapor phase to 500 °C: implications for As transport and fractionation in low-density crustal fluids and volcanic gases. *Geochim. Cosmochim. Acta* **66**, 3453–3480.

Pokrovski G. S., Roux J. and Harrichoury J. C. (2005) Fluid density control on vapor–liquid partitioning of metals in hydrothermal systems. *Geology* **33**, 657–660.

Radcliffe D. and McSween H. Y. (1969) Copper zoning in pyrite from Cerro de Pasco, Peru: a discussion. *Am. Mineral.* **54**, 1216–1217.

Radcliffe D. and McSween H. Y. (1970) Copper zoning in pyrite from Cerro de Pasco, Perú: reply. *Am. Mineral.* **55**, 527–528.

Raymond O. L. (1996) Pyrite composition and ore genesis in the Prince Lyell copper deposit, Mt Lyell mineral field, western Tasmania, Australia. *Ore Geol. Rev.* **10**, 231–250.

Reich M., Kesler S. E., Utsunomiya S., Palenik C. S., Chryssoulis S. L. and Ewing R. C. (2005) Solubility of gold in arsenian pyrite. *Geochim. Cosmochim. Acta* **69**, 2781–2796.

Reich M., Utsunomiya S., Kesler S. E., Wang L. M., Ewing R. C. and Becker U. (2006) Thermal behavior of metal nanoparticles in geologic materials. *Geology* **34**, 1033–1036.

Reich M., Chryssoulis S. L., Deditius A., Palacios C., Zúñiga A., Weldt M. and Alvear M. (2010) "Invisible" silver and gold in supergene digenite (CuS). *Geochim. Cosmochim. Acta* **74**, 6157–6173.

Reich M., Hough R. M., Deditius A., Utsunomiya S., Ciobanu C. L. and Cook N. J. (2011) Nanogeoscience in ore systems research: principles, methods, and applications. *Ore Geol. Rev.* **42**, 1–5.

Richards J. (2003) Tectono-magmatic precursors for porphyry Cu–(Mo–Au) deposit formation. *Econ. Geol.* **98**, 1515–1533.

Rusk B. G., Reed M. H. and Dilles J. H. (2008) Fluid inclusion evidence for magmatic-hydrothermal fluid evolution in the porphyry copper–molybdenum deposit at Butte, Montana. *Econ. Geol.* **103**, 307–334.

Savage K. S., Tingle T. N., O'Day P. A., Waychunas G. A. and Bird D. K. (2000) Arsenic speciation in pyrite and secondary weathering phases, Mother Lode gold district, Tuolumne County, California. *Appl. Geochem.* **15**, 1219–1244.

Schmid-Beurmann P. and Bente K. (1995) Stability properties of CuS_2–FeS_2 solid solution series pyrite type. *Mineral. Petrol.* **53**, 333–341.

Seedorff E., Dilles J. H., Proffett J. M., Einaudi M. T., Zurcher L., Stavast W. J. A., Johnson D. A. and Barton M. D. (2005) Porphyry deposits: characteristics and origin of hypogene features. *Econ. Geol.* **100th Anniversary volume**, 251–298.

Shimazaki H. and Clark L. A. (1970) Synthetic FeS_2–$CuFe_2$ solid solution and fukuchilite-like minerals. *Can. Mineral.* **10**, 648–664.

Sillitoe R. H. (2000) Gold-rich porphyry deposits: descriptive and genetic models and their role in exploration and discovery. *Rev. Econ. Geol.* **13**, 315–345.

Sillitoe R. H. (2010) Porphyry copper systems. *Econ. Geol.* **105**, 3–41.

Simon G., Huang H., Penner-Hahn J. E., Kesler S. E. and Kao L. S. (1999) Oxidation state of gold and arsenic in gold-bearing arsenian pyrite. *Am. Mineral.* **84**, 1071–1079.

Simon A. C., Pettke T., Candela P. A., Piccoli P. M. and Heinrich C. (2007) The partitioning behavior of As and Au in a haplogranite – vapor at magmatic conditions in sulfur-free and sulfur-bearing systems. *Geochim. Cosmochim. Acta* **71**, 1764–1782.

Simon A. C., Pettke T., Candela P. A., Piccoli P. M. and Heinrich C. (2008) The partitioning behavior of silver in a vapor–brine–rhyolite melt assemblage. *Geochim. Cosmochim. Acta* **72**, 1638–1659.

Sung Y. H., Brugger J., Ciobanu C. L., Pring A., Skinner W. and Nugus M. (2009) Invisible gold in arsenian pyrite and arsenopyrite from a multistage Archaean gold deposit: Sunrise Dam, Eastern Goldfields Province, Western Australia. *Mineral. Deposita* **44**, 765–791.

Ulrich T. and Heinrich C. A. (2002) Geology and alteration geochemistry of the porphyry Cu–Au deposit at Bajo de la Alumbrera, Argentina. *Econ. Geol.* **96**, 1719–1742.

Ulrich T., Long D. G. F., Kamber B. S. and Whitehouse M. J. (2011) In situ trace element and sulfur isotope analysis of pyrite in a paleoproterozoic gold placer deposit, Pardo and Clement Townships, Ontario, Canada. *Econ. Geol.* **106**, 667–686.

Van Geen A., Adkins J. F., Boyle E. A., Nelson C. H. and Palanques A. (1997) A 120 yr record of widespread contamination from mining of the Iberian pyrite belt. *Geology* **25**, 291–294.

Vaughan J. P. and Kyin A. (2004) Refractory gold ores in Archaean greenstones, Western Australia: mineralogy, gold paragenesis, metallurgical characterization and classification. *Mineral. Mag.* **68**, 255–277.

Wang Q., Xu J. F., Jian P., Bao Z. W., Zhao Z. H., Li C. F., Xiong X. L. and Ma J. L. (2006) Petrogenesis of adakitic porphyries in an extensional tectonic setting, Dexing, South China: implications for the genesis of porphyry copper mineralization. *J. Petrol.* **47**, 119–144.

William-Jones A. E. and Heinrich C. A. (2005) Vapor transport of metals and the formation of magmatic-hydrothermal ore deposits. *Econ. Geol.* **100th Anniversary Volume**, 1287–1312.

Yamaguchi K. and Ohmoto H. (2006) Evidence from sulfur isotope and trace elements in pyrites for their multiple post-depositional processes in uranium ores at the Stanleigh Mine, Elliot Lake, Ontario, Canada. *GSA Memoirs* **198**, 143–156.

Zhao J. H., Zhou M. F., Yan D. P., Zheng J. P. and Li J. W. (2011) Reappraisal of the ages of Neoproterozoic strata in South China: No connection with the Grenvillian orogeny. *Geology* **39**, 299–302.

Zhou X. M., Sun T., Shen W. Z., Shu L. S. and Niu Y. L. (2006) Petrogenesis of Mesozoic granitoids and volcanic rocks in South China: A response to tectonic evolution. *Episodes* **29**, 26–33.

Associate editor: W. Uwe Reimold